nature materials

SUPPLEMENTARY INFORMATION

https://doi.org/10.1038/s41563-018-0268-1

In the format provided by the authors and unedited.

Three-dimensional printing of piezoelectric materials with designed anisotropy and directional response

Huachen Cui[1], Ryan Hensleigh[2], Desheng Yao[1], Deepam Maurya[1], Prashant Kumar[1], Min Gyu Kang[1], Shashank Priya[1,3] and Xiaoyu (Rayne) Zheng[1,2]*

[1]Department of Mechanical Engineering, Virginia Tech, Blacksburg, VA, USA. [2]Macromolecules Innovation Institute, Virginia Tech, Blacksburg, VA, USA. [3]Materials Research Institute, Pennsylvania State University, University Park, PA, USA. *e-mail: raynexzheng@vt.edu

3D printing of piezoelectric materials with designed anisotropy and directional response

Authors: *Huachen Cui[1], Ryan Hensleigh[2], Desheng Yao[1], Deepam Maurya[1], Prashant Kumar[1], Min Gyu Kang[1], Shashank Priya[1,3], Xiaoyu (Rayne) Zheng[1,2*]*

Author Affiliations:

[1]*Department of Mechanical Engineering, Virginia Tech, Blacksburg, Virginia 24061, USA*

[2]*Macromolecules Innovation Institute, Virginia Tech, Blacksburg, Virginia 24061, USA*

[3]*Materials Research Institute, Penn State, University Park, PA 16802, USA*

***Corresponding author**: X. Zheng, Email: raynexzheng@vt.edu

Contents

SI. 1 Quantification of the difference between theoretical prediction and FEA results

Theoretical prediction of the dimensionless d constants

We first calculated the analytical results of the N=5 structure with different relative orientations of projected struts denoted in manuscript. To determine the analytical results of $\bar{d}_{3M}$, we followed the analytical model in the manuscript. The effective electric displacement and effective stress are:

$$D_n^{eff} = \frac{1}{V}\sum_{i=1}^{N}\int_{V_i} D_n^{(i)} dV_i \quad (S1.1)$$

$$\sigma_{KL}^{eff} = \frac{1}{V}\sum_{i=1}^{N}\int_{V_i} \delta_{Kk}\delta_{Ll}\sigma_{kl}^{(i)} dV_i \quad (S2.2)$$

where $\sigma_{kl}^{(i)}$ and $D_n^{(i)}$ ($n\ k\ l = 1,2,3$) are, respectively, the stress matrix and electric displacement vector of each strut in the global coordinate system, V and V_i are, respectively, the volume of the unit cell and of the i-th strut. According to Eq. 1 in the manuscript, d_{3M}^{eff} in matrix becomes

$$\begin{Bmatrix} d_{31}^{eff} \\ d_{32}^{eff} \\ d_{33}^{eff} \end{Bmatrix} = \begin{Bmatrix} \frac{D_3^{eff}}{\sigma_{11}} \\ \frac{D_3^{eff}}{\sigma_{22}} \\ \frac{D_3^{eff}}{\sigma_{33}} \end{Bmatrix} \quad (S1.3)$$

As shown in Fig. S1, the architecture design with symmetric constraints (e.g., same projection pattern in 1-3 and 2-3 plane) significantly reduces the complexity of Eq. (S1.1) and Eq. (S1.2) by grouping identical struts (i.e., identical electric displacement contribution, identical strut length, diameter, and cross-sectional shape). This allows the evaluation of the contribution of different type of struts to effective electric displacement field. As shown in Fig. S2a, two groups of identical

struts are identified: i). strut parallel to 3-axis ($\vec{L}_5$); ii) struts that are not parallel to the 3-axis ($\vec{L}_1, \vec{L}_2, \vec{L}_3, \vec{L}_4$). It is therefore sufficient to represent the group by one strut in each group.

Below we derive a closed-form expression of effective piezoelectric charge constant d as a function of spatial orientations of ligaments within a unit cell. We started from force equilibrium of a single strut and established a local coordinate system (x-y-z coordinate system) and the global coordinate system (1-2-3). The parameters of these two-coordinate systems are shown in Fig. S2b. The x-axis of the local coordinate system is parallel to strut space vector $\vec{L}_i$. The axial stress $\sigma_{pq}^{(i)}$ is firstly calculated in the local coordinate system (x-y-z), and then transformed to the global coordinate system $\sigma_{kl}^{(i)}$ $(k, l = 1,2,3)$. The correlation between the stress matrix in the local coordinate system and the global coordinate system is achieved through the transformation matrix N^i as:

$$\sigma_{kl}^{(i)} = N^i \sigma_{pq}^{(i)} (N^i)^T \quad (S1.4)$$

. Similarly, the electrical displacement contribution of each strut can be expressed as:

$$D_n^{(i)} = d_{nkl} \sigma_{kl}^{(i)} = d_{nkl} N^i \sigma_{pq}^{(i)} (N^i)^T \quad (S1.5)$$

Hence, we derived the expression of the transformation matrix N^i correlating the local coordinate system to the global coordinate system to calculate the effective electrical displacement D_n^{eff} and effective stress σ_{KL}^{eff}, and further, calculate the effective charge constants.

According to Euler's rotation theorem, any coordinate system transformation may be described using three angles. In this situation, the force components that we considered is an axial force ($\vec{F}_x$), which is in alignment with strut space vector $\vec{L}_i$, and shear force ($\vec{F}_z$), which is perpendicular to the strut space vector $\vec{L}_i$. Here, we derive the transformation matrix via rotating the 1-axis of the global

coordination system such that it overlaps with the x-axis of the local coordinate system of a single strut $\vec{L}_i$ and then define the rest of the coordinates. By doing this, the transformation matrix for 1st-4th and 5th strut can be written as:

$$\begin{bmatrix} N_{11}^i & N_{12}^i & N_{13}^i \\ N_{21}^i & N_{22}^i & N_{23}^i \\ N_{31}^i & N_{32}^i & N_{33}^i \end{bmatrix} = \begin{bmatrix} \cos\theta_3\cos\theta_4 & -\sin\theta_3 & -\cos\theta_3\sin\theta_4 \\ \sin\theta_3\cos\theta_4 & \cos\theta_3 & -\sin\theta_3\sin\theta_4 \\ \sin\theta_4 & 0 & \cos\theta_4 \end{bmatrix} \quad (S1.6)$$

$$\begin{bmatrix} N_{11}^5 & N_{12}^5 & N_{13}^5 \\ N_{21}^5 & N_{22}^5 & N_{23}^5 \\ N_{31}^5 & N_{32}^5 & N_{33}^5 \end{bmatrix} = \begin{bmatrix} 0 & 0 & 1 \\ 0 & 1 & 0 \\ -1 & 0 & 0 \end{bmatrix} \quad (S1.7)$$

For d_{33}^{eff}, regrouping Eq. (S1.1) and (S1.2) by identical struts yields

$$D_3^{eff} = \frac{1}{V}\{d_{31}\ \ d_{32}\ \ d_{33}\}\left(4A_1|L_1|\begin{Bmatrix}\sigma_{11}^1\\ \sigma_{22}^1\\ \sigma_{33}^1\end{Bmatrix} + A_5|L_5|\begin{Bmatrix}\sigma_{11}^5\\ \sigma_{22}^5\\ \sigma_{33}^5\end{Bmatrix}\right) \quad (S1.8)$$

$$\sigma_{33} = \frac{1}{V}(4A_2|L_2|\sigma_{33}^1 + A_5|L_5|\sigma_{33}^5) \quad (S1.9)$$

Consider a remote compressive stress σ along z direction that is applied to the infinite lattice structure consists of the node unit. From force equilibrium, the total force applied on the node unit F can be given as:

$$F = 4\sigma L^2\sin^2\theta_3\cos^2\theta_4 \quad (S1.10)$$

Under this z-direction stress σ, the vertical strut ($\vec{L}_5$) is subject to normal stress, while other strut ($\vec{L}_1, \vec{L}_2, \vec{L}_3, \vec{L}_4$) are subject to a combination of normal and shear stresses. From equilibrium, the local stress matrix of strut group ($\vec{L}_1, \vec{L}_2, \vec{L}_3, \vec{L}_4$) is:

$$\sigma_{pq}^{(i)} = \frac{\sigma L^2}{A_1}\begin{bmatrix} \sin^2\theta_3\cos^2\theta_4 sin\theta_4 & 0 & \sin^2\theta_3\cos^3\theta_4 \\ 0 & 0 & 0 \\ \sin^2\theta_3\cos^3\theta_4 & 0 & 0 \end{bmatrix} \qquad (S1.11)$$

Similarly, the local stress matrix of vertical strut ($\vec{L}_5$) is:

$$\sigma_{pq}^{(5)} = \frac{4\sigma L^2}{A_5}\begin{bmatrix} \sin^2\theta_3\cos^2\theta_4 & 0 & 0 \\ 0 & 0 & 0 \\ 0 & 0 & 0 \end{bmatrix} \qquad (S1.12)$$

By substituting Eq. (S1.11) and (S1.12) into Eq. (S1.4), the global stress matrix is obtained. Then substitute Eq. (S1.8) and (S1.9) into Eq. (S1.3), we obtain d_{33}^{eff} for the $N = 5$ structure as:

$$d_{33}^{eff} = \frac{-\cos^2\theta_3\cos^2\theta_4\sin\theta_4 d_{31} - \sin^2\theta_3\cos^2\theta_4\sin\theta_4 d_{32} + (\sin\theta_4(1+\cos^2\theta_4)+1)d_{33}}{2+2\sin\theta_4} \quad (S1.13)$$

Similarly, d_{31}^{eff} could be obtained as:

$$d_{31}^{eff} = \frac{-\cos^3\theta_3\cos^2\theta_4\sin\theta_4 d_{31} - \sin^2\theta_3\cos\theta_3\cos^2\theta_4\sin\theta_4 d_{32} + \cos\theta_3\sin\theta_4(1+\cos^2\theta_4)d_{33}}{2\sin\theta_3\cos\theta_4} (S1.14)$$

Due to symmetry, $d_{31}^{eff} = d_{32}^{eff}$.

It should be noted that since the bending stress is symmetric to the neutral surface of the strut (integration of bending stress over cross-section area is zero), it does not contribute to the effective electric displacement and charge constants.

Electric displacement manipulation via screw angle in 2D projection patterns

As shown in Fig. S2, the plane angles θ_1, θ_2 and θ_3 obtained from projection pattern as:

$$\theta_1 = \theta_2 = \theta - 90°, \theta_3 = 45°$$

The space angle θ_4 could be expressed as:

$$\theta_4 = \arctan\left(\sqrt{2}\tan(\theta - 90°)\right)$$

From the two equations above, all the angles θ_1, θ_2, θ_3 and θ_4 invoked in the analytical analysis could be tuned through adjusting angle θ in the projection pattern. Therefore, the stress matrix of each strut in the global coordinate system could be conveniently manipulated through configuring its orientation in the projection pattern. Subsequently, the effective electric displacement and effective charge constants are manipulated through the configuration of strut orientation in the projection patterns.

Comparison between the theoretical prediction and the FEA results

ABAQUS 6.14 was used to conduct the finite element analysis on all the designs shown in Fig. S1. Comparison between analytical derivations and finite element analysis shows great agreement between the two. We listed the calculated results in Fig. S1. The minimal difference between the analytical model and FEA result can be explained by the difference of stress calculation of vertical struts during calculation of d_{31}^{eff} and d_{32}^{eff}. The axial stress on the vertical strut $\vec{L}_5$ is considered zero in the analytical derivation of equilibrium state[1], whereas the FEM analysis indicated the stress within vertical strut still takes approximately 5% of that of the diagonal strut ($\vec{L}_1, \vec{L}_2, \vec{L}_3, \vec{L}_4$) due to stress transferred from the node.

Benchmark with other modeling schemes and finite element models

We have benchmarked our modeling scheme with other modeling schemes as well as finite element models for specific cases. The benchmarking is presented in two parts: compare with other modeling scheme and compare with other finite element models on established geometries.

Comparison with other modeling schemes

We first benchmarked our approach with other modeling schemes on a classic, bulk piezoelectric composite. One of the commonly used modeling approaches is the micromechanics theory for composite. Micromechanics theory[2] invoked in previous literature has been utilized for several problems, including the uncoupled mechanical and electric behavior of composites[3], and coupled electroelastic property of composites. In this method, the effective electroelastic moduli are obtained by considering the volume average of piezoelectric field variables.

Here we utilize our approach to analyze effective charge displacement and compare it with a classical 3-3 piezoelectric composite model that has been widely studied by Bowen et al[4], and Rittenmyer et al.[5] using the volume averaging approach. The structure of the piezoelectric composite is sketched in Fig. S5a&b. The composite consists of two phases: active PZT ceramics and inactive polymer. The referenced approach assumes that the piezoelectric material parallel to the poling direction (z-direction) is fully poled (as indicated by the shaded volumes in Fig. S5a). The remaining columns perpendicular to the poling direction (x-direction and y-direction) are considered unpoled.

In the volume averaging model, the effective charge constant is the summation of the product of each phase's charge constant and its volume fraction within the composite. Rittenmyer et.al[5] derived the effective piezoelectric charge constant of the classical composite shown in Fig. S5 as:

$$d_{33}^{eff} = \frac{v^{d33PZT} d_{33}^{PZT}}{v^{d33PZT} + (1 - v^{d33PZT}) \frac{S_{33}^{PZT}}{S_{33}^{polymer}}} \quad (S1.15)$$

$$d_{31}^{eff} = v^{d31PZT} d_{31}^{PZT} \quad (S1.16)$$

where S_{33}^{PZT} and $S_{33}^{polymer}$ are, respectively, the compliance of PZT ceramic and polymer, v^{d33PZT} and v^{d31PZT} are volume fraction of PZT ceramic that contributes to d_{33}^{eff} and d_{31}^{eff}, respectively.

We then analyze this classical composite model using our modeling scheme via deriving the effective electric displacement {D} distribution. In the case shown in Fig. S5a&b, only the poled piezoelectric portion (shaded volume in Fig. S5a&b) contributes to the electric displacement. Meanwhile, the only stress component for PZT ceramic and polymer are σ_{33}^{PZT} and $\sigma_{33}^{polymer}$. Hence Eq. 2 (Methods), combined with piezoelectric properties of the base material of each ligament in the Method and Material section can be rewritten as:

$$D_3^{eff} = \frac{L^2(L+l_1)\sigma_{33}^{PZT} d_{33}^{PZT}}{(L+l_1)(L+l_2)^2} \qquad (S1.17)$$

where l_1, l_2 and L are defined as the length and width of the columns, as shown in Fig. S5. Simplify Eq. S1.17 and replace σ_{33}^{PZT} with compliance, S_{33}^{PZT}, and strain, ε_{33}, we get:

$$D_3^{eff} = \frac{v^{d33PZT}}{S_{33}^{PZT}} d_{33}^{PZT} \varepsilon_{33} \qquad (S1.17)$$

$$\sigma_{33}^{eff} = \left(\frac{v^{d33PZT}}{S_{33}^{PZT}} + \frac{1 - v^{d33PZT}}{S_{33}^{polymer}} \right) \varepsilon_{33} \qquad (S1.19)$$

The effective charge constant d_{33}^{eff} is:

$$d_{33}^{eff} = \frac{v^{d33PZT} d_{33}^{PZT}}{v^{d33PZT} + (1 - v^{d33PZT}) \frac{S_{33}^{PZT}}{S_{33}^{polymer}}} \qquad (S1.20)$$

Similarly, d_{31}^{eff} is calculated as:

$$d_{31}^{eff} = v^{d31PZT} d_{31}^{PZT} \qquad (S1.21)$$

Therefore, the effective charge constants derived from our analytical model is identical to the one given in the reference using the benchmark approach. This benchmarking verifies the validity of our analytical modeling scheme via calculating the effective electric displacement.

Compare with other finite element models

We also benchmarked our analytical approach with an existing finite element model on piezoelectric open foam. Challagulla and Venkatesh[6] developed a numerical model based on an idealized unit cell to characterize the complete electro-mechanical response for porous piezoelectric foams. The idealized unit cell model is shown in Fig. S5d. All the shaded ligaments are PZT phase and the remaining volume of the unit cell is porosity. Cross-section areas of all ligaments, A, are the assumed to be uniform. Poling direction is 3-direction in Fig. S5d. Based on the numerical results in the paper, the normalized charge constant vector is $\{\bar{d}_{31} \quad \bar{d}_{32} \quad \bar{d}_{33}\} = \{-0.348 \quad -0.348 \quad 0.870\}$.

Here, we analyzed this open-cell model using our analytical modeling scheme on calculating effective charge displacement contributions from ligaments. The portion of the piezoelectric material that contributes to electrical displacement in calculating d_{31} and d_{33} are the shaded volumes shown in Fig. S5e&f, respectively. Electric charge displacement maps from the unit cell patterns are plotted as white arrows in the shaded ligament.

For d_{31}^{eff} , assume a uniform stress σ_{11} is applied in 1-direction. The stress component on shaded ligaments is σ_{11}. The effective electrical displacement is calculated as:

$$D_3^{eff} = \frac{1}{V}\sum_{i=1}^{N}\int_{V_i} D_3^{(i)} dV_i \qquad (S1.22)$$

where L_i and L are defined as the length of the struts, as shown in Fig. S5. The effective stress is

$$\sigma_{11}^{eff} = \sigma_{11} \qquad (S1.23)$$

. Hence the d_{31}^{eff} is calculated as:

$$d_{31}^{eff} = \frac{4Ad_{31}}{(2L_i + L)^2} \qquad (S1.24)$$

Due to symmetry, $d_{32}^{eff} = d_{31}^{eff}$. Similarly,

$$d_{33}^{eff} = \frac{4Ad_{33}}{(2L_i + L)^2} \qquad (S1.25)$$

The dimensionless charge constant vector calculated from our analytical modeling scheme is $\{\bar{d}_{31} \quad \bar{d}_{32} \quad \bar{d}_{33}\} = \{-0.332 \quad -0.332 \quad 0.883\}$, matching reasonably close to the finite element model used in the benchmark literature[6].

SI. 2 Expanded architectures and their d_{3M} distributions

We also demonstrate our design scheme and calculate the distribution of d_{3M}^{eff} of *N*=12 structure, as shown in Fig. S3. We denoted the local and global stresses of each strut in vector form. The stretching-dominated deformation mechanism gives rise to negligible bending and shear stresses, it is easier to express the local and global stresses in vector form. To determine d_{3M}^{eff}, rewriting Eq. (2) in a matrix form and in terms of strut stress for the convenience of analytical calculation, we obtain:

$$D_3^{eff} = \frac{1}{V}\sum_{i=1}^{N} A_i\left|\vec{L}_i\right| \cdot [d_{31}^i \quad d_{32}^i \quad d_{33}^i \quad d_{34}^i \quad d_{35}^i \quad d_{36}^i] \begin{bmatrix} T_{11}^i & T_{12}^i & \dots & T_{16}^i \\ T_{21}^i & T_{22}^i & \dots & T_{26}^i \\ \vdots & \vdots & \ddots & \vdots \\ T_{61}^i & T_{62}^i & \dots & T_{66}^i \end{bmatrix} \begin{Bmatrix} \sigma_{xx}^i \\ \sigma_{yy}^i \\ \sigma_{zz}^i \\ \sigma_{xy}^i \\ \sigma_{xz}^i \\ \sigma_{yz}^i \end{Bmatrix} \qquad (S2.1)$$

$$\begin{Bmatrix}\sigma_{11}\\ \sigma_{22}\\ \sigma_{33}\\ \sigma_{12}\\ \sigma_{13}\\ \sigma_{23}\end{Bmatrix} = \frac{1}{V}\sum_{i=1}^{N} A_i\left|\vec{L}_i\right| \cdot \begin{bmatrix} T_{11}^i & 0 & \dots & 0 \\ 0 & T_{22}^i & \dots & 0 \\ \vdots & \vdots & \ddots & \vdots \\ 0 & 0 & \dots & T_{66}^i \end{bmatrix} \begin{Bmatrix}\sigma_{xx}^i\\ \sigma_{yy}^i\\ \sigma_{zz}^i\\ \sigma_{xy}^i\\ \sigma_{xz}^i\\ \sigma_{yz}^i\end{Bmatrix} \quad (S2.2)$$

, where $\{\sigma_{xx}^i \quad \sigma_{yy}^i \quad \sigma_{zz}^i \quad \sigma_{xy}^i \quad \sigma_{xz}^i \quad \sigma_{yz}^i\}^T$ is the vector form in terms of the local coordinate of σ_{pq}^i, and T^i is the stress transformation matrix from the local coordinate system to the global coordinate system (Fig. S4). The architecture design with symmetric constraints significantly reduces the complexity of Eq. ($S2.2$) and Eq. ($S2.3$) by grouping identical struts (i.e. identical electric displacement contribution, identical strut length, diameter and cross-sectional shape). This allows the evaluation of contribution of different types of struts to the effective electric displacement field. Finally, according to Eq. (1), d_{3M}^{eff} in matrix form becomes:

$$\begin{Bmatrix} d_{31}^{eff} \\ d_{32}^{eff} \\ d_{33}^{eff} \end{Bmatrix} = \begin{Bmatrix} \frac{D_3^{eff}}{\sigma_{11}} \\ \frac{D_3^{eff}}{\sigma_{22}} \\ \frac{D_3^{eff}}{\sigma_{33}} \end{Bmatrix} \quad (S2.3)$$

For *N*=12 structure, only axial stresses are considered due to its stretch-dominated nature. Eq. (S2.1)-(S2.3) then lead to the results of d_{3M}^{eff} (only M=1, 2, 3 is of interest) of *N*=12 structure. For d_{31}^{eff}, the parent material piezoelectric charge constants are identical for each strut (Table. S2). Eq. (S2.1) and Eq. (S2.2) then reduce to:

$$D_3^{eff} = \frac{1}{V}\sum_{i=1}^{12} A_i\left|\vec{L}_i\right| \cdot \left(d_{31}T_{11}^i + d_{32}T_{21}^i + d_{33}T_{31}^i\right)\sigma_{xx}^i \quad (S2.4)$$

$$\sigma_{11} = \frac{1}{V}\sum_{i=1}^{N} A_i\left|\vec{L}_i\right| \cdot T_{11}^{i}\sigma_{xx}^{i} \quad (S2.5)$$

. Three groups of identical struts are identified (Fig. S3a): i) struts parallel to 1-3 plane subjected to axial compression ($\vec{L}_2, \vec{L}_4, \vec{L}_{10}, \vec{L}_{12}$); and ii) struts parallel to 1-2 plane subjected to axial compression ($\vec{L}_5, \vec{L}_6, \vec{L}_7, \vec{L}_8$); and iii) struts parallel to 2-3 plane subjected to axial tension ($\vec{L}_1, \vec{L}_3, \vec{L}_9, \vec{L}_{11}$). It is therefore sufficient to represent the group by one strut in each group. Therefore, regrouping Eq. (S2.4) and (S2.5) by identical struts yields:

$$D_3^{eff} = \frac{1}{V}\{d_{31} \quad d_{32} \quad d_{33}\}\left(4\begin{Bmatrix} T_{11}^2 \\ T_{21}^2 \\ T_{31}^2 \end{Bmatrix} A_2\left|\vec{L}_2\right|\sigma_{xx}^2 + 4\begin{Bmatrix} T_{11}^5 \\ T_{21}^5 \\ T_{31}^5 \end{Bmatrix} A_5\left|\vec{L}_5\right|\sigma_{xx}^5 + 4\begin{Bmatrix} T_{11}^1 \\ T_{21}^1 \\ T_{31}^1 \end{Bmatrix} A_1\left|\vec{L}_1\right|\sigma_{xx}^1\right) \quad (S2.6)$$

$$\sigma_1 = \frac{1}{V}\left(4T_{11}^2 A_2\left|\vec{L}_2\right|\sigma_{xx}^2 + 4T_{11}^5 A_5\left|\vec{L}_5\right|\sigma_{xx}^5 + 4T_{11}^1 A_1\left|\vec{L}_1\right|\sigma_{xx}^1\right) \quad (S2.7)$$

, where, from geometric relationships,

$$\begin{cases} T_{11}^2 = \dfrac{\sqrt{2}}{2}\cos\dfrac{1}{2}\theta \\ T_{21}^2 = \dfrac{\sqrt{2}}{2}\cos\dfrac{1}{2}\theta \\ T_{31}^2 = \sin\dfrac{1}{2}\theta\cos\dfrac{1}{2}\theta \\ T_{11}^5 = \dfrac{1}{2} \\ T_{21}^5 = \dfrac{1}{2} \\ T_{31}^5 = 0 \\ T_{11}^1 = 0 \\ T_{21}^5 = \dfrac{1}{2} \\ T_{31}^5 = \dfrac{1}{2} \end{cases} \quad (S2.8)$$

, also, $\left|\vec{L}_2\right| = \left|\vec{L}_1\right| = \frac{\sqrt{2}}{\cos\frac{1}{2}\theta}\left|\vec{L}_5\right|$, $A_2 = A_5 = A_1$. In this case, $\theta = \angle\vec{l}_3^1\vec{l}_{11}^1 = \theta'$ (Fig. S3b). Using nodal force equilibrium, we obtain the relationships between axial stresses of three types of struts: $\sigma_{xx}^2 = -\sigma_{xx}^1 = \frac{\sqrt{2}}{2}\frac{1}{\cos\frac{1}{2}\theta}\sigma_{xx}^5$. Thus, substituting Eq. (S2.6) and (S2.7) into Eq. (S2.3), we obtain d_{31}^{eff} for *N*=12 structure as:

$$d_{31}^{eff} = \frac{\left(\frac{\sqrt{2}}{2}\cos\frac{1}{2}\theta + \frac{1}{2}\cos^2\frac{1}{2}\theta - \frac{1}{2}\right)(d_{32} + d_{31}) + \left(\sin\frac{1}{2}\theta\cos\frac{1}{2}\theta - \frac{1}{2}\right)d_{33}}{\frac{\sqrt{2}}{2}\cos\frac{1}{2}\theta + \frac{1}{2}\cos^2\frac{1}{2}\theta} \quad (S2.9)$$

. Due to the symmetry, $d_{31}^{eff} = d_{32}^{eff}$. Similarly, d_{33}^{eff} can be obtained as:

$$d_{33}^{eff} = \frac{\left(cos^2\frac{1}{2}\theta - \frac{\sqrt{2}}{12sin\frac{1}{2}\theta - 4cos\frac{1}{2}\theta}\right)(d_{31} + d_{32}) + 2sin^2\frac{1}{2}\theta d_{33}}{\sqrt{2}sin\frac{1}{2}\theta} \quad (S2.10)$$

Eq. (S2.9) and (S2.10) show that the variation of θ changes the effective piezoelectric charge constants by varying the contribution of material properties d_{31}, d_{32} and d_{33}.

A list of some other designed node units and their normalized effective piezoelectric charge constants are estimated and shown in Table S1. The 3D node unit with dissimilar projection patterns and its results are also shown. Despite that the projection patterns are 3-strut, with different skew angles between adjacent struts defined as $\theta_1 = \angle\vec{l}_1^1\vec{l}_2^1$ and $\theta_2 = \angle\vec{l}_1^2\vec{l}_2^2$, they yields a distribution of d_{3M} with $d_{31} \neq d_{32}$ (3-strut dissimilar projection patterns, Table S1). Another node unit with 3-strut pattern on 1-3 plane and 5-strut pattern on 2-3 plane is also illustrated (3-strut/5-strut dissimilar projection patterns, Table S1). This type of design further enhances the tunability of piezoelectric properties by utilizing the dissimilar projection patterns design.

Another superposition structure by summing two 3-strut projection patterns is also generated (6-strut projection patterns, Table S1). d_{32} and d_{31} are nearly zero for $\theta = 60°$ due to the counteractive contributions of two groups of struts: i) struts paralleled to 1-3 plane; and ii) struts paralleled to 2-3 plane. d_{33} is predicted as negative at $\theta = 30°$ while $d_{31} = d_{32} > 0$, reaching a quadrant different from other designs (Table S1). The node units with 6-strut dissimilar projection patterns are also shown to verify its d_{3M} distribution in (- + -) and (+ - +) quadrants (6-strut dissimilar projection patterns, Table S1).

SI. 3 PZT particle properties

In the present work, we used commercial piezoelectric material particles (APC 850). The size of the PZT particles was measured by dynamic light scattering (Malvern Zetasizer Nano ZS), and we found the average diameter to be 220.9 nm in acetonitrile solvent. The properties of the PZT particle are summarized in Table S2. The Curie temperature of the PZT (APC 850), used in this work, was 360°C.

SI. 4 Particle uniformity in the polymer matrix

Our PZT particle surface functionalization, resin mixing method and printing process collectively ensure the uniformity of the spatial distribution and no-settling occurred during the printing, even in the presence of high-volume loading (Fig. S6). Surface functionalization helps achieve uniformity in the liquid resin by creating a sterically hindered surface, a common technique in nanomaterial synthesis[7]. During the functionalization procedure, PZT particles were ultrasonically dispersed in the deionized water with glacial acetic acid, after which the surface functionalization agent was added. The mixture was then refluxed while stirring for 5h. Particles were cleaned by centrifugation, discarding the supernatant, and then dispersing in pure ethanol for at least two cycles. The dried particles were mixed with photo-curable resin using a high energy ball mill

(EMAX, Retsch) for 30 minutes to ensure the mixture is uniform. During the printing procedure, the strong, irreversible bonding of the nanoparticle surface acrylates and the polymer matrix acrylates maintains the uniform dispersion within the printed parts. An average printing takes less than 1.5 hours to finish, and there is no noticeable particle sedimentation over that period of time for the resin mixed with functionalized particles, as shown in Fig. S6.

To confirm the uniformity of the printed parts, we printed a series of beams with the same overall size (0.3mm x 0.3mm x 5mm) and different particle loadings within the polymer matrix. We performed scanning electron microscopy (SEM, FEI Quanta 600FEG) on these beams, and recorded the morphology of the surface of these beams. The SEM micrographs are shown in Fig. S7. We did not find any visible variation in the spatial distribution of the PZT particles in the polymer matrix.

SI. 5 Characterization of the effect of particle functionalization

To characterize the effect of functionalization, we prepared composite samples with varying degree of functionalization between nanoparticles and polymer matrix and probed their effect on the piezoelectric properties at different particle volume loading. Our experiments confirmed that the fully functionalized systems provide the "upper bound" of properties obtainable for a particular volume fraction of the piezoelectric particles while the partially functionalized particle systems provide less.

In Fig. S8a&b, we show the Fourier-transform Infrared Spectroscopy (FTIR) of thoroughly cleaned functionalized PZT particles with different intimal loadings of the surface agent or reaction times. The spectrum focuses on the carbonyl and alkene of the acrylate surface groups nominally at 1710 cm^{-1} and 1630 cm^{-1}, respectively. It shows the functionalization level can be varied by the surface linker loading or reaction time.

We functionalized PZT particles with 0wt% ~ 150wt% surface linker loadings. The particles with different functionalization levels were mixed with the UV curable resin with 3% to 30% volume loadings (equivalent to 18.8wt%~76.3wt% loading), and were used for fabricating cuboid samples (8mm by 8mm by 2 mm). As-fabricated samples were tested using the same apparatus described in SI. 9. The d_{33} constants of the samples are summarized in Fig. S8c. For the low particle loading (3vol%) composite, the d constant is nearly zero without functionalization, and increases with the functionalization level until the particles are fully functionalized. The same trend was observed for the high particle loading (30vol%, i. e., 76.3wt%) composite, i.e., the d constant increases from ~50pC/N to ~100pC/N with fully functionalized nanoparticles.

To investigate the effect of functionalization at different particle loadings, cuboid samples having the same dimensions with 3vol%~30vol% PZT particles with and without functionalization were fabricated and tested. The results are shown in Fig. S8d. Within 30vol% loading, the performance of the piezocomposite is increased by the surface functionalization of the piezo particles. It can be noted that in the absence of functionalization, the baseline piezoelectric response is increased with higher volume loadings.

SI. 6 Resolution and optimization of the fabrication process

The current system to process piezoelectric feedstock achieves minimum printable 3D feature size of ~20um in the transverse direction, which is determined by pixel resolution of the DMD array and the reduction lens. The resolution in vertical direction is controlled by the layer thickness during the printing. To ensure the layer thickness is well-controlled, layer recoating process and the cure depth of the resins with higher nanoparticle loadings are modeled and experimentally characterized during our study.

After one layer of resin is cured, a recoating process is followed. The stage on which the lattices were printed is moved for a layer thickness to recoat resin for the printing of next layer. While resin with low particle loading can be recoated within a short time between each layer, high particle loadings resin suffers from its dramatically increased viscosity as such it cannot flow into the gap uniformly within a reasonable time. To ensure the high particle loading resins can be uniformly and efficiently recoated, we used tape-casting method[8] to recoat the resin, as shown in Fig. S9a&b. As shown in Fig. S9, once a layer is cured, the Z stage moves. Right after the movement, an extruder squeezes a small amount of the resin on the oxygen permeable membrane and a doctor blade produces a thin resin film on the membrane. Then the Z stage moves back, leaving a flat layer height resin.

Optimization of the blade height to control thickness

In our process, only a small amount of resin for each layer was dispensed. We designed the blade position such that the gap between the blade head and the substrate is sufficient to ensure 1) dispensed nanoparticle resin can spread out the printing area, 2) the spread resin height is higher than exposure thickness. Fig. S9c illustrates the blade design criteria to ensure adequate nanoparticle resin quality. The blade height must satisfy

$$\frac{2h_L A'}{A} < h_{blade} < \frac{Ah_d}{A'}$$

where A is the cross-section area of the dispensed resin, h_d is the thickness of the dispensed resin and A' is the cross-section area of the recoated resin (Fig. S9c).

We tested the recoating quality of the resins having different particle loadings and the results are summarized in Fig. S10. The particle loading that can yield a relatively uniform layer with high quality (without pores) for final fabrication was found to be 50vol% (~ 88 wt%) in our study.

Curing depth of highly loaded piezoelectric monomers

Another important parameter affecting the layer thickness is the cure depth of the resin. In SLA process, the curing depth is related to the Beer-Lambert law, which is formulated as[9]:

$$Z_{ct} = \frac{1}{\alpha}\ln\left(\frac{E}{E_c}\right) \qquad (S6.1)$$

where α is the resin absorption coefficient, E and E_c are the actual and critical exposure respectively. E can be controlled by the UV light intensity or exposure time.

For resins loaded with particles, the UV light is scattered or absorbed when it travels through the resin. The absorption coefficient of the resins, α, becomes quite large in highly particle loaded resins, and can be formulated as[10-12]:

$$\alpha \sim \frac{3S\emptyset}{2d} \qquad (S6.2)$$

$$S \sim \left(\frac{\Delta n}{n_0}\right)^2 \left(\frac{d}{\lambda}\right)^2 \qquad (S6.3)$$

where S is a constant related to the scattering efficiency of the particles, d is the mean diameter of particles, $\emptyset$ is the volume fraction of the particle in the high particle loading resin, n_0 is the refractive index of the rein, Δn is the refractive indice difference between the particle and the solution and λ is the light wavelength.

Empirically, we found that the layer thickness has to be set less than half of the cure depth in order to ensure tight bonding force between neighboring layers. This creates challenge as higher particle loadings nanoparticles cause reduction of the resin penetration depth based on Eq. (S6.1) due to higher resin absorption constant. For each particle loading a series of exposure time and dosage must be carefully conducted to characterize the penetration depth of the loading. Additionally, our

enclosed system allows accurate control of oxygen concentration (typically below 1%), which helps to increase the cure depth of the resin via prevention of oxygen inhibition mechanism[13,14] and promote more photopolymerization. To find the dosage and exposure time for sufficient cure depth (twice of the layer thickness) of resins with different particle loadings, an identical circle array pattern with various exposure time and dosage is used to characterize the cure depth. Excess resin is then wiped away and the thickness of the printed dot is measured under microscope. As shown in Fig. S11a, the number of cured disk patterns decreases as the particle loading increases under the same exposure profile, which indicates different exposure parameters are needed for each loading concentrations.

As an example, we plotted the working curve of the resin with 40vol% loading particles in Fig. S11b. The light intensity we used is the highest intensity of the projection system, which is ~20W. Various exposure time is used to achieve different curing depth. The curing depth is 30um with 16s exposure time and start to saturate after 16s. So we used 15um as the layer thickness during the printing of the 40vol% particle loading resin.

SI. 7 Tailorable compliance, sensing and energy harvesting capability

Fig. S12 shows the compliance measurement of the metamaterial having different relative densities and monomers with different elasticity. These metamaterials were compressed using INSTRON-5944 with 0.05/min strain rate. The compliance is calculated from the reciprocal of the slope of the stress-strain curve (Table S3). The testing results show that these group of piezoelectric metamaterials possess tailorable compliance over three orders of magnitude. Fig. S13 shows the voltage output of a flexible piezoelectric metamaterial when it’s attached onto a curved surface and compressed by fingers (MOVIE S1).

Besides, we show two demos with a flexible 3D architected skin-like sensor (MOVIE S2) and impact energy harvesting apparatus to further validate the potential of the architected piezoelectric materials.

3D architected flexible tactile sensor

As shown in Fig. S14 a~b, the 3D architected piezoelectric metamaterial can be stretched and bent by fingers with ease without fracture, and are highly conformable to different shapes, e. g., fingers and joints, suggesting their applicability in wearable devices and skin like sensors. As a demonstration, a ring-like sensor was prepared and tested to show the voltage output during the folding and unfolding process of the author's little thumb, as shown in Fig. S14c~d. When the finger was folded, the architected sensor is under 3-3 working mode, which means the pressure is applied along the 3-direction (polarization direction) and the voltage is generated on the electrodes along the 3-direction. Fig. S14e displays the real-time waveforms of the folding and unfolding pressure pulse recorded from the sensor (MOVIE S2).

Energy generation and stability of the piezocomposite energy harvester

To demonstrate the energy harvesting capability of our piezocomposite, we used the piezoelectric metamaterial to harvest energy from the external impacts. An architected film with 40% porosity was printed using the 50vol% PZT composite, as shown in the inset of Fig. S15a. The as-fabricated sample was then poled with a 4V/um electric field under room temperature for 1 hour. After poling, two silver electrodes with cables were attached to the sample to form the piezoelectric energy harvester.

A rectifier and charge storage circuit including the bridge rectifier, a capacitor (C=100μF), a switch and the LED array were connected to the piezocomposite energy harvester, as shown in Fig. S15a&c. A shaker with integrated force sensor in contact with the surface of the energy harvester

applied a small cyclical loading (~1N peak to peak) on the sample. The generated voltage was measured through myDAQ, while the generated charge was stored in the capacitor. The voltage output of the harvester was relatively stable over 360000 cycles, as shown in Fig. S15b. We observed a small variation in the generated voltage ($\delta V = 7{\sim}8\%$), showing the stability of our piezoelectric composite. The stored energy was then used to illuminate a pattern formed by 13 LEDs. Fig. S15d shows the illumination of the LEDs after turning on the switch between the capacitor and the LED pattern. The LEDs are illuminated for 0.5s with a 2.85V voltage (U) on the capacitor.

SI. 8 Polarization method and results

We used standard corona poling method[15] that has been commonly used for poling PZT composites[16]. A schematic of the poling fixture is shown in Fig. S16. We performed poling process at the elevated temperature (~110^{o}C) for some of our samples in contact mode and did not observe any appreciable change in the physical properties. As such, we performed the poling process at the room temperature for most of the samples. The corona process is a non-contact poling process and it involves application of very high field through a needle, while the sample is attached below on the grounded plate. Under the application of high field, the surrounding air is ionized. These ions are collected on the top surface of the sample generating the effective field across the thickness of the sample. This resulted aligning the dipoles (i.e., poling) in the direction of the applied field. The applied voltage during the poling process is 32kV and the height of needle from the sample surface is 2cm.

Our testing results for tactile mapping also confirmed good uniformity of the poling process. We prepared a N=12, Θ=90^{o} lattice with four electrodes attached at different positions across the lattice surface (Fig. S17) The electrodes were connected to 4 resistors (10MΩ) with a data acquisition

system for reading output voltages from different positions. Identical, calibrated loadings (2.2N) from a shaker (Model V203, Ling dynamic systems LTD) were applied along 3-direction on the electrodes, the peak voltage generated from four positions were nearly identical, which indicates uniform polarization in lattice upon poling.

SI. 9 Assembly and calibration of the piezoelectric testing apparatus for 3D piezoelectric metamaterials

The piezoelectric metamaterials were first activated by a polarization process in strong electric fields as described in the Method section. After the poling was completed, the electrodes coated with the composite resin was attached to the sample to eliminate triboelectric effects. The sample was compressed with the electrodes to ensure the sample is fully attached to the electrodes (Fig. S19a). Leads were connected to the electrodes through copper wires. The sample was put on the top of a high precision force sensor (APPLIED MEASUREMENTS LTD. DBCR-20N-002-000) from which the impact force was read, and a shaker (LING DYNAMIC SYSTEMS, LTD. V203) having a sawtooth voltage input was used to applied impact on the sample. One side of the electrodes was grounded while another side is connected to the circuit shown in Fig. S19b[17]. The voltage readout from the circuit was recorded by a data acquisition system (LabView myDAQ) and multiplied by the reference capacitor to calculate the charge generated from the sample. Fig. S19d shows the response of the non-polarized and polarized samples with ~0.5N periodic impact force.

The measurement of piezoelectric coefficient was calibrated using standard calibration piezoelectric sample provided by APC International, Ltd. Wide-Range Piezo d_{33} Tester Meter. Fig. S19c shows the generated charge as a function of impact force for two standard samples having 540pC/N and 175pC/N standard piezoelectric materials. The slope equals the piezoelectric

constant. The error of measured results is below 5% comparing with values reported from the manufacturer. Zero voltage output of the non-polarized sample indicates the triboelectric effects have been eliminated from the system.

SI. 10 Piezoelectric voltage constant and hydrostatic figure of merit

While the mechanical properties (strength, stiffness) in architected metamaterials scale down with volume fractions, creating volume fractions (low relative density) in these piezoelectrics invoke many unique advantages for piezoelectric properties as compared to their bulk material. As seen in Eq. S1.13 and S1.14, d constants are not sensitive to relative density in the linear elastic regime, therefore at low volume fractions, their mechanical-electro coupling factors remain consistent with higher volume fractions of the same architecture. Our study has found that, the piezoelectric voltage constant, g, another key piezoelectric property constant, increases with the reduction of relative density and outperform their original starting material. g constant is the most relevant piezoelectric constant characterizing electro-mechanical coupling for transducer and sensor performance[18]. The g_{33} constants is related with d_{33} and electric permittivity via,

$$g_{33} = \frac{d_{33}}{\varepsilon_{33}}$$

where d_{33} and ε_{33} are the piezoelectric charge constant and permittivity in the 3-direction, respectively. The permittivity of the lattices has a nearly linear relationship with the relative density and can be calculated using the following equation[19]:

$$\varepsilon_{33} = [\bar{\rho}(k_c - 1) + 1]\varepsilon_0$$

where $\bar{\rho}$ is the relative density of the lattices, k_c is the dielectric constant of the bulk composite and ε_0 is the permittivity of vacuum. For the bulk composite, the relative density can be considered as 1. The relationship between the permittivity and relative density was further verified using a

commercial capacitance meter (KEYSIGHT, E4990A). The capacitance of the lattices was measured, and the permittivity can be calculated from the following equation:

$$\varepsilon_{33} = \frac{Cd}{A}$$

where C is the capacitance of the lattice, d is the distance between the electrodes and A is the cross-section area of the lattice.

As a result, it can be seen that the lower electric permittivity inherent within the piezoelectric metamaterials contributes to the increased piezoelectric voltage constant g. For example, the g_{33} constant of the N=12, Θ=90° lattices increases as the relative density decreases, as plotted in Fig. 3d in our original manuscript. Therefore, the voltage constants of the low relative density lattices outperform that of the bulk composites, indicating superior sensing capabilities.

Additionally, these micro-architected metamaterials outperform its base material and other piezoelectric materials regarding their hydrostatic properties. For hydrophone applications, an important parameter is the hydrostatic figure of merit (FOM)[20], which defines the material's suitability for underwater sonar applications,

$$FOM = d_h \cdot g_h \ (Pa^{-1})$$

where,

$$d_h = d_{33} + (d_{32} + d_{31})(CN^{-1})$$

$$g_h = \frac{d_h}{\varepsilon}(Vm^{-1})$$

As shown in Fig. S20, the FOM of the piezoelectric metamaterials can be tuned in a large range by tuning the piezoelectric anisotropy via architecture and exceeding other piezoelectric materials

and other piezoelectric foams[20-27]. This beneficial property is attributed to, i) through changing the micro-architectures, the anisotropy of the d and h constants of these piezoelectric metamaterials can be tuned from {-, -, +} to {+, +, +} leading to the increase of d_h. ii) higher overall $g_h$at lower densities as compared to the base material and other piezoelectric materials, attributed to the low electric permitivity ε. This benfit of lower densities (e.g., lower permitivity) also validates predictions obtained from piezoelectric foam structures.

SI. 11 Details of the material selection chart

The envelope of the "Present work" in Fig. 3e will be enlarged if all configurations of metamaterials are mapped out based on the tunable range of the *relative density*, *configuration of the micro-architectures*, as well as *stiffness* of the binding monomers. Furthermore, the composite we used includes a large range of particle loading (3vol%~50vol%) and as a result, their density varies with particle loading. We normalize the $|d_{33}|$ with density to exclude the density variation with different particle loadings and highlight the benefit of consistent $|d_{33}|$ constant with decreasing relative density unique to piezo-active metamaterials, in contrast to the commonly known degradation of mechanical properties at lower relative density in structural metamaterials.

Fig. S21 plots the approximate envelop with most architectures and materials considered here. There are three factors affecting the tunable property envelope. The first factor is the tuned stiffness from the binding monomers employed in our study, marked as "stiff" and "flexible", respectively. The second factor is the nodal connectivity of the architectures. Based on the nodal connectivity which affects their effective modulus of the metamaterial, we group them into bending dominated and stretching dominated. The third factor is the screw angle of these structures, which affects the d_{33} constant as well as compliance.

The boundary and scaling relationships on effective charge constants, modulus and effect of relative density are estimated using the method as described in SI. 1 and SI. 2. The compliance is calculated based on the following equation:

$$J = \alpha \bar{\rho}^{-\beta} J_s$$

where α is a pre-factor, β is the scaling factor, $\bar{\rho}$ is the relative density and J_s is the compliance of the base materials. α is related to the screw angle and varies from 0.2~5 for different structures[28,29]. For the bend-dominated structure, β falls within the range of 2.1~2.3[30,31]. For the stretch-dominated structure, β is set within the range of 1.1~1.3[28,32]. J_s has two values as we change the polymer matrix.

In the logarithmic coordinate system, the scaling between the dimensionless effective charge constant and the compliance of the structural group is a constant and can be calculated by:

$$\frac{\Delta \log(\left|d_{33}^{eff}\right|/\rho)}{\Delta \log(J)} = \frac{1}{\beta}$$

Based on our fabrication capability for the range of relative densities, we set the range of the relative density as 5%~45%. Particle loading we used for mapping the envelope is set at 3vol%. The envelope is mapped out in Fig. S21 using dashed lines and shaded areas in red. The straight dashed lines represent structures with the same structural group, screw angle and base material. Experimental results on the scaling relationships two categories, N=12, Θ=90° and N=5, Θ=120° structures are plotted.

SI. 12 Fracture test of the piezoelectric metamaterial containing a crack

Here, we conducted center cracked tension (CCT)[33] test to evaluate the fracture toughness of the metamaterials. We conducted CCT tests on the N=5, Θ=120° design, with outer dimensions

defined by L (length), W (width) and T (thickness) and an initial through-thickness notch of length ~W/2, as shown in Fig. S22a. The relative density of the samples varies from 10% to 32% and all samples were fabricated using our elastic-brittle composite (PEGDA-PZT) with 3vol% PZT and tested with Instron 5944. The applied tensile load, P, versus load-line displacement, v, of a piezoelectric sample with a central notch at a relative density $\bar{\rho} = 28\%$ is shown in Fig. S22b. After an initially linear $P - v$ response, a peak load, P_c, was reached followed by a load drop, which was caused by the fracture of the struts right in front of the crack tip. The fracture toughness, K_{Ic}, of the samples was measured from the measured critical load, P_c, values from samples with relative density ranging from 10% to 32%. Here we compared the fracture energy (G_{Ic})[34] of these metamaterials of relative density ranging from 10% to 32%, with those of other piezoelectric relavant materials and porous materials[35-37]. Due to the very limited reported fracture toughness data on existing piezoelectric materials and foams to date, we are only able to compare the fracture energy of these samples with a few types of porous materials agains their relative density, as shown in Fig. S22d. The high fracture energy of the metamaterial shows its potential as energy absorbing materials when compared to other porous materials. The effective tensile strength of the samples with the same design and relative density range was measured by uniaxial tensioning the samples (with the same overall dimension) without crack, plotted in Fig. S22c.

SI. 13 Impact mapping of the piezoelectric bridge infrastructure

We first predict the impact point on the bridge-like structure by using four known displacements at the piers and relative positions among piers. A wave propagation and attenuation theory within the planar boundary (the deck) is utilized. The amplitude of the induced response at a given position within the boundary could be simplified to follow an exponential attenuation relation as:

$$u = Ce^{-Dr} \quad (S13.1)$$

, where u is the induced response amplitude (displacement) of the point of interest (at the pier), C and D is a coefficient depending on the amplitude of the impulse and the damped frequency of the deck, r is the distance between the pier and the impact point. To obtain the displacements at four piers, the proportional relationship between peak voltage output and pier displacement is used due to the linear deformation of the piers:

$$u = A \cdot V_{peak} \quad (S13.2)$$

, where A is the coefficient of proportionality, V_{peak} is the peak voltage output at the pier. Combining Eq. (S13.1) and Eq. (S13.2) yields the direct relationship between voltage output and distance r. A coordinate system is then set originating from pier 1, and therefore, the coordinates of each pier is defined (Fig. S23). Let the unknown impact point as (x, y), with four r's in terms of voltage outputs given by Eq. (S13.1) and Eq. (S13.2), four relationships between r's and (x, y) are denoted as:

$$r_k^2 = (x - x_k)^2 + (y - y_k)^2 \quad (S13.3)$$

, where r_k is the distance between *k*-th pier and the impact point, x_k and y_k are coordinates of the *k*-th pier, $k = 1{\sim}4$. With four circles defined by Eq. (S13.3), one intersect point (i.e., impact point (x, y)) is determined while the maximum displacement induced by the impact force is also determined. By knowing the impact point, using Eq. (S13.1), the strain at each point on the deck normalized by the maximum strain is thus solved.

SI. 14 Material properties used in FEA

The input parameters are taken from experimentally obtained properties of the bulk composite material. The parameters are:

Density: $\rho = 1.36 \times 10^3 kg/m^3$

Elastic property :$E_1 = E_2 = 770MPa, E_3 = 480MPa, \nu_{12} = 0.46, \nu_{23} = 0.64, \nu_{13} = 0.37, G_{12} = 257MPa, G_{23} = G_{13} = 480MPa$

Dielectric permittivity: $\epsilon_{11} = \epsilon_{22} = 2.6 \times 10^{-10} F/m,\ \epsilon_{33} = 1.2 \times 10^{-10} F/m$

Piezoelectric charge constant: $d_{15} = d_{24} = 70pC/N$, $d_{31} = d_{32} = -15pC/N$, $d_{33} = 52pC/N$, the other $d_{ij} = 0$.

Supplementary Movies

Movie S1| Flexible metamaterial for energy conversion Hand tapping induced voltage response of the N=12 flexible piezoelectric metamaterial conformally attached onto a curved surface.

Movie S2| Flexible 3D ring-like piezo-sensor A ring-like sensor was prepared and tested to show the signal generated during the folding and unfolding process of human figures.

Movie S3| Directional voltage response Real-time voltage outputs of piezoelectric metamaterials comprised of N=5 node unit with $\theta = 75°$, $90°$, and $120°$ under impact coming from 1, 2, and 3 directions.

Movie S4| Drop-weight impact absorption and self-sensing Drop-weight impact test on the piezoelectric metamaterial comprised of N=12 node units.

Movie S5| Directionality sensing Real-time voltage output maps of the piezoelectric infrastructure comprised of stacked architectures under impact coming from 1, 2, and 3 directions.

References

1 Yang, L., Harrysson, O., West, H. & Cormier, D. Mechanical properties of 3D re-entrant honeycomb auxetic structures realized via additive manufacturing. *Int J Solids Struct* **69-70**, 475-490 (2015).

2 Huang, J. H. & Kuo, W. S. Micromechanics determination of the effective properties of piezoelectric composites containing spatially oriented short fibers. *Acta Mater* **44**, 4889-4898 (1996).

3 Glushanin, S., Topolov, V. Y. & Krivoruchko, A. V. Features of piezoelectric properties of 0-3 PbTiO3-type ceramic/polymer composites. *Mater Chem Phys* **97**, 357-364 (2006).

4 Bowen, C. R., Perry, A., Stevens, R. & Mahon, S. Analytical and numerical modelling of 3-3 piezoelectric composites. *Integr Ferroelectr* **32**, 1025-1034 (2001).

5 Rittenmyer, K., Shrout, T., Schulze, W. A. & Newnham, R. E. Piezoelectric 3-3 Composites. *Ferroelectrics* **41**, 323-329 (1982).

6 Challagulla, K. S. & Venkatesh, T. A. Electromechanical response of piezoelectric foams. *Acta Mater* **60**, 2111-2127 (2012).

7 Sperling, R. A. & Parak, W. J. Surface modification, functionalization and bioconjugation of colloidal inorganic nanoparticles. *Philos T R Soc A* **368**, 1333-1383 (2010).

8 Jabbari, M. & Hattel, J. Bingham plastic fluid flow model in tape casting of ceramics using two doctor blades - analytical approach. *Mater Sci Tech Ser* **30**, 283-288 (2014).

9 Tumbleston, J. R. *et al.* Continuous liquid interface production of 3D objects. *Science* **347**, 1349-1352 (2015).

10 Song, X. *et al.* Piezoelectric component fabrication using projection-based stereolithography of barium titanate ceramic suspensions. *Rapid Prototyping J* **23**, 44-53 (2017).

11 Griffith, M. L. & Halloran, J. W. Stereolithography of ceramics. *Proceedings of the Sixth International Conference on Rapid Prototyping - 1995*, 25-34 (1995).

12 Griffith, M. L. & Halloran, J. W. Freeform fabrication of ceramics via stereolithography. *J Am Ceram Soc* **79**, 2601-2608 (1996).

13 Zheng, X. Y. *et al.* Design and optimization of a light-emitting diode projection micro-stereolithography three-dimensional manufacturing system. *Rev. Sci. Instrum* **83**, 125001 (2012).

14 Cui, H., Hesleigh, R., Chen, H. & Zheng, X. Fabrication and Size-dependent Mechanical Properties of Three-dimensional Microarchitected, High-temperature Ceramic Metamaterials. *Journal of Material Research* **33,** 360-371 (2017).

15 Kim, H. et al. Integrated 3D printing and corona poling process of PVDF piezoelectric films for pressure sensor application. *Smart Mater Struct* **26,** 085027 (2017).

16 Min, Y. H., Lee, K. S., Yoon, C. S. & Do, L. M. Surface morphology study of corona-poled thin films derived from sol-gel processed organic-inorganic hybrid materials for photonics applications. *J Mater Chem* **8**, 1225-1232 (1998).

17 Kim, K. *et al.* 3D Optical Printing of Piezoelectric Nanoparticle - Polymer Composite Materials. *Acs Nano* **8**, 9799-9806 (2014).

18 Jaffe, H. & Berlincourt, D. A. Piezoelectric Transducer Materials. *Pr Inst Electr Elect* **53**, 1372-1386 (1965).

19 Lifson, M. L., Kim, M. W., Greer, J. R. & Kim, B. J. Enabling Simultaneous Extreme Ultra Low-k lin Stiff, Resilient, and Thermally Stable Nano-Architected Materials. *Nano Lett* **17**, 7737-7743 (2017).

20 Kara, H., Ramesh, R., Stevens, R. & Bowen, C. R. Porous PZT ceramics for receiving transducers. *Ieee T Ultrason Ferr* **50**, 289-296 (2003).

21 Liu, W. *et al.* Processing and Properties of Porous PZT Ceramics from Particle-Stabilized Foams via Gel Casting. *J Am Ceram Soc* **96**, 1827-1831 (2013).

22 Bowen, C. R., Perry, A., Lewis, A. C. F. & Kara, H. Processing and properties of porous piezoelectric materials with high hydrostatic figures of merit. *J Eur Ceram Soc* **24**, 541-545 (2004).
23 Marselli, S. *et al.* Porous piezoelectric ceramic hydrophone. *J Acoust Soc Am* **106**, 733-738 (1999).
24 Yang, A. K., Wang, C. A., Guo, R. & Huang, Y. Microstructure and Electrical Properties of Porous PZT Ceramics Fabricated by Different Methods. *J Am Ceram Soc* **93**, 1984-1990 (2010).
25 Zhang, Y., Chen, L. J., Zeng, J., Zhou, K. C. & Zhang, D. Aligned porous barium titanate/hydroxyapatite composites with high piezoelectric coefficients for bone tissue engineering. *Mat Sci Eng C-Mater* **39**, 143-149 (2014).
26 Guo, R., Wang, C. A. & Yang, A. K. Effects of pore size and orientation on dielectric and piezoelectric properties of 1-3 type porous PZT ceramics. *J Eur Ceram Soc* **31**, 605-609 (2011).
27 Liu, W., Du, L. J., Wang, Y. Z., Yang, J. L. & Xu, H. Effects of foam composition on the microstructure and piezoelectric properties of macroporous PZT ceramics from ultrastable particle-stabilized foams. *Ceram Int* **39**, 8781-8787 (2013).
28 Zheng, X. Y. *et al.* Ultralight, Ultrastiff Mechanical Metamaterials. *Science* **344**, 1373-1377 (2014).
29 Yang, L., Harrysson, O., West, H. & Cormier, D. Modeling of uniaxial compression in a 3D periodic re-entrant lattice structure. *J Mater Sci* **48**, 1413-1422 (2013).
30 Deshpande, V. S., Ashby, M. F. & Fleck, N. A. Foam topology bending versus stretching dominated architectures. *Acta Mater* **49**, 1035-1040 (2001).
31 Gibson, L. J. & Ashby, M. F. *Cellular Solids: Structure and Properties*. (Cambridge University Press, Cambridge, 1999).
32 Dong, L., Deshpande, V. & Wadley, H. Mechanical response of Ti-6Al-4V octet-truss lattice structures. *Int J Solids Struct* **60-61**, 107-124 (2015).
33 Tada, H., Paris, P. C. & Irwin, G. R. *The stress analysis of cracks handbook.* (Del Rdearch Corporation, St. Louis, 1977).
34 Johnson, F. A., Glover, A. P. & Radon, J. C. Fracture Toughness and Fracture Energy Measurements on Aluminum-Alloys. *Eng Fract Mech* **8**, 381-390 (1976).
35 Mcintyre, A. & Anderton, G. E. Fracture Properties of a Rigid Polyurethane Foam over a Range of Densities. *Polymer* **20**, 247-253 (1979).
36 Lam, D. C. C., Lange, F. F. & Evans, A. G. Mechanical-Properties of Partially Dense Alumina Produced from Powder Compacts. *J Am Ceram Soc* **77**, 2113-2117 (1994).
37 Wouterson, E. M., Boey, F. Y. C., Hu, X. & Wong, S. C. Specific properties and fracture toughness of syntactic foam: Effect of foam microstructures. *Compos Sci Technol* **65**, 1840-1850 (2005).

Supplementary Figures and Table

	Projection (Identical)	Electric displacement map			3D Node unit	Theoretical prediction {d_{31}, d_{32}, d_{33}}	Numerical calculation			FEA results {d_{31}, d_{32}, d_{33}}
							31 mode	32 mode	33 mode	
a	N=5, Θ=15° (- - +)					{-0.69, -0.69, 0.19}				{-0.70, -0.70, 0.16}
b	N=5, Θ=30° (- - +)					{-0.68, -0.68, 0.27}				{-0.67, -0.67, 0.30}
c	N=5, Θ=75° (- - +)					{-0.46, -046, 0.76}				{-0.44, -0.44, 0.79}
d	N=5, Θ=90° (~0 ~0 +)					{-0.28, -0.28, 0.92}				{-0.25, -0.25, 0.94}
e	N=5, Θ=120° (+ + +)					{0.48, 0.48, 0.73}				{0.46 0.46, 0.77}
f	N=5, Θ=150° (+ + +)					{0.64, 0.64, 0.43}				{0.63, 0.63, 0.45}
g	N=5, Θ=165° (- - +)					{0.69, 0.69, 0.24}				{0.68, 0.68, 0.27}

Figure S1| The comparison between analytical results, experiment results and numerical results of the N=5 lattices.

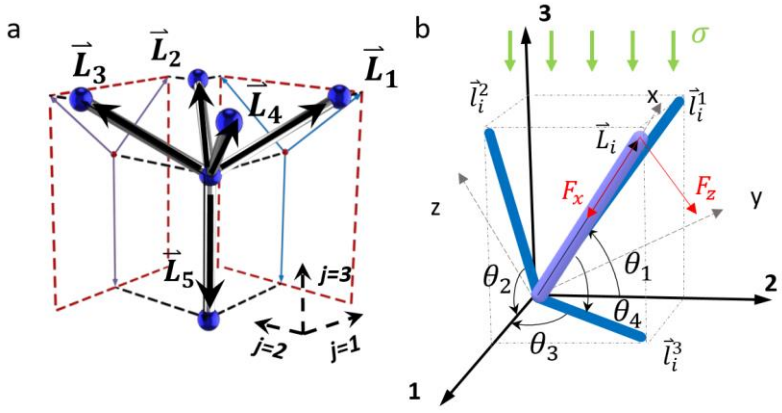

Figure S2| a) Schematic of the N=5 design. b) Schematic of a single strut with two coordinate systems.

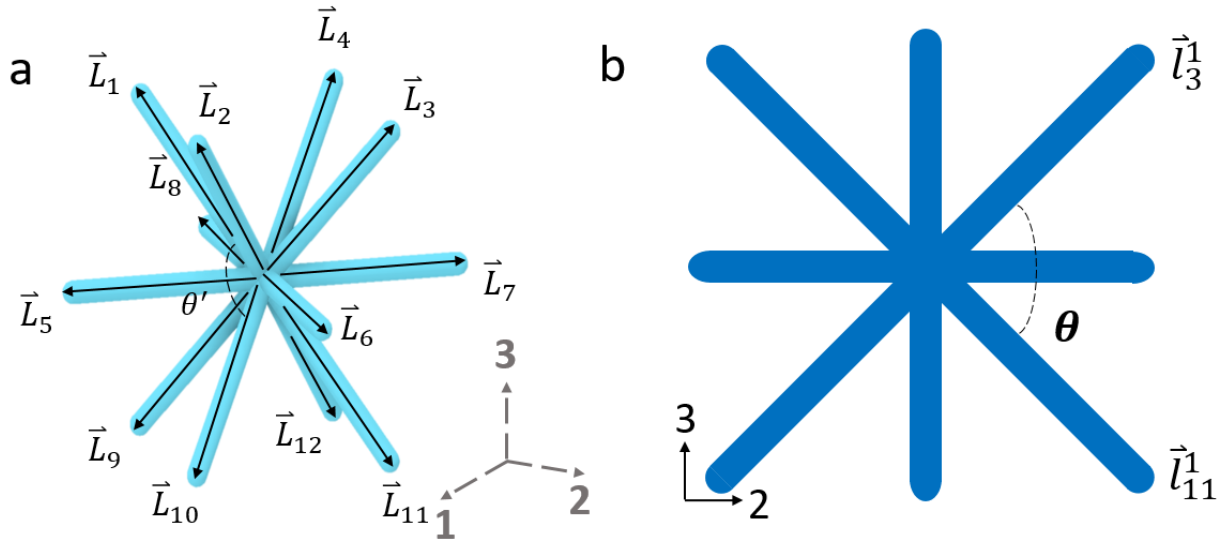

Figure S3| (a) *N*=12 designs with its corresponding projection patterns (b) on 2-3 plane for analytical calculation.

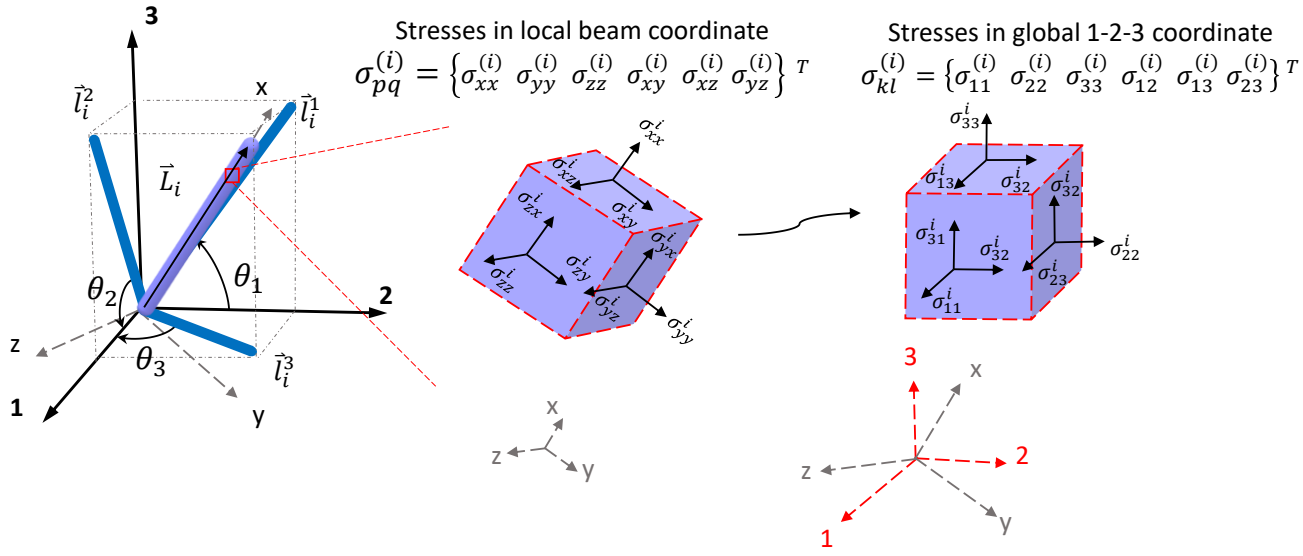

Figure S4| 3D strut defined in global and local coordinate systems for developing unit node model.

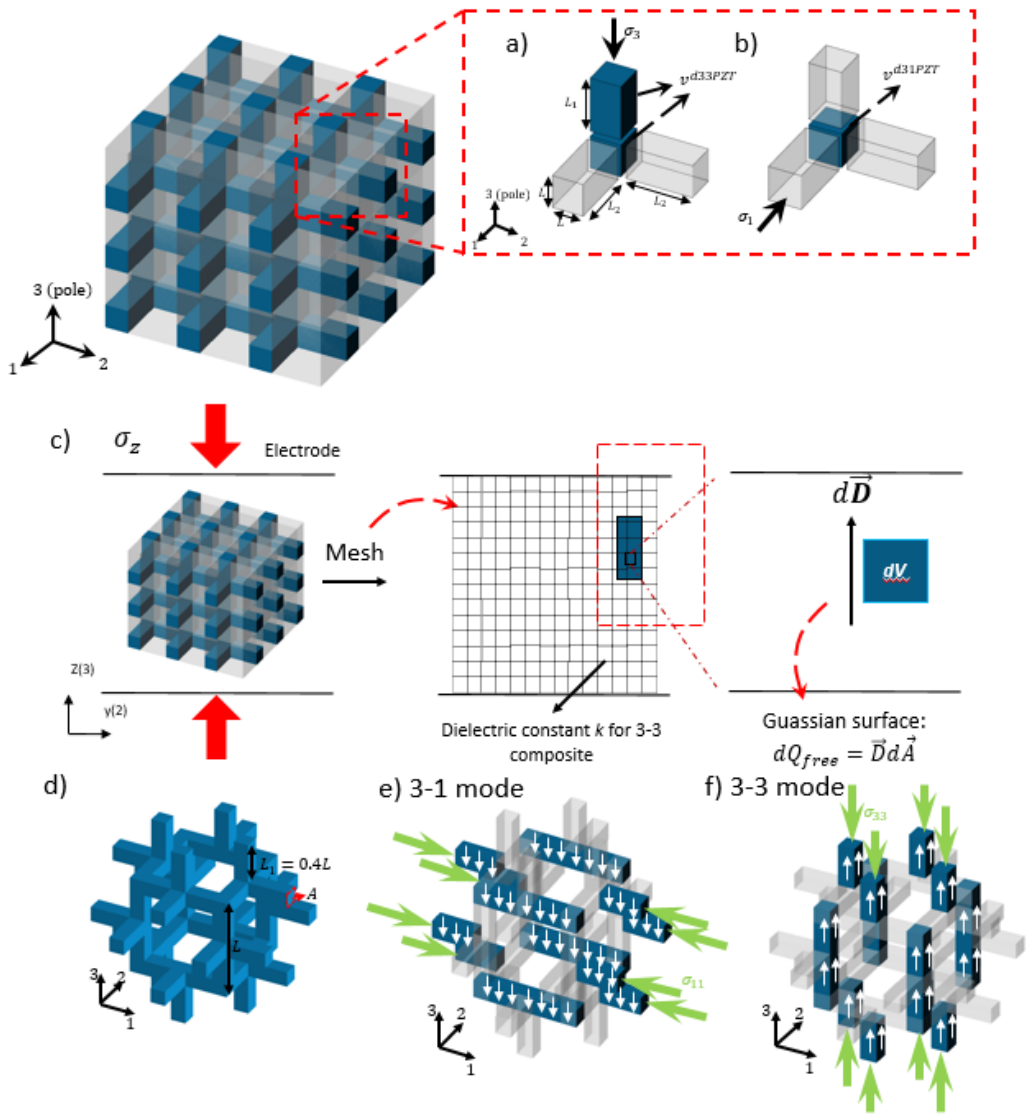

Figure S5| Benchmark study. a~b) The lattice and unit cell model of the piezoelectric composite. The shaded volumes in a) indicate struts contributing to effective permittivity and d33 of the composite. The shaded volume in b) indicates struts contributing to the d31 coefficient of the composite. c) Schematics for analyzing the composite using the theoretical model presented in our manuscript. d) Schematics of the open foam unit cell. e~f) Contribution map of the struts under different stress mode (3-1 mode and 3-3 mode).

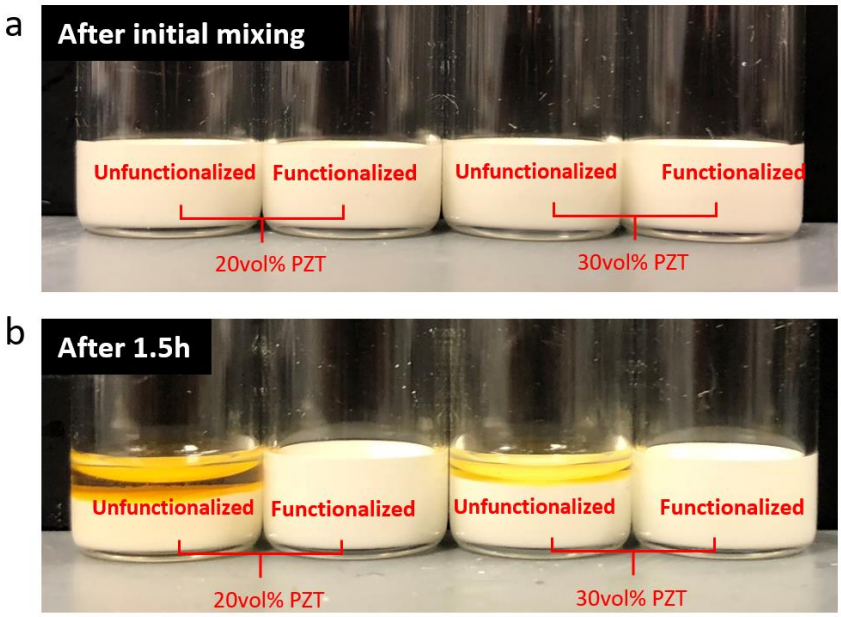

Figure S6| Optical images of the resins mixed with unfunctionalized or functionalized particles a) after initial mixing and b) after 1.5h.

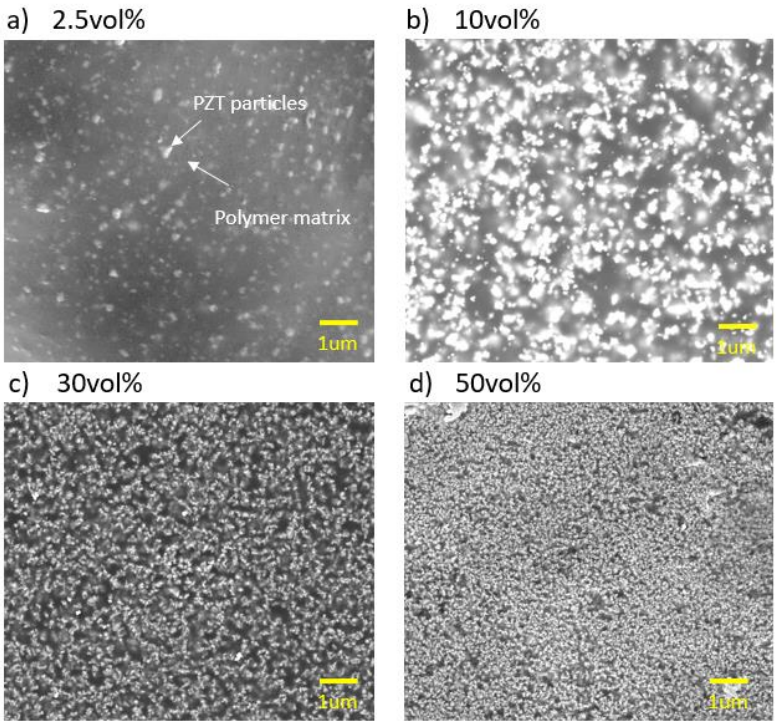

Figure S7| The SEM micrographs of the cross section areas of the composite having a) 2.5vol%, b) 10vol% c) 30vol% d) 50vol% particle loading.

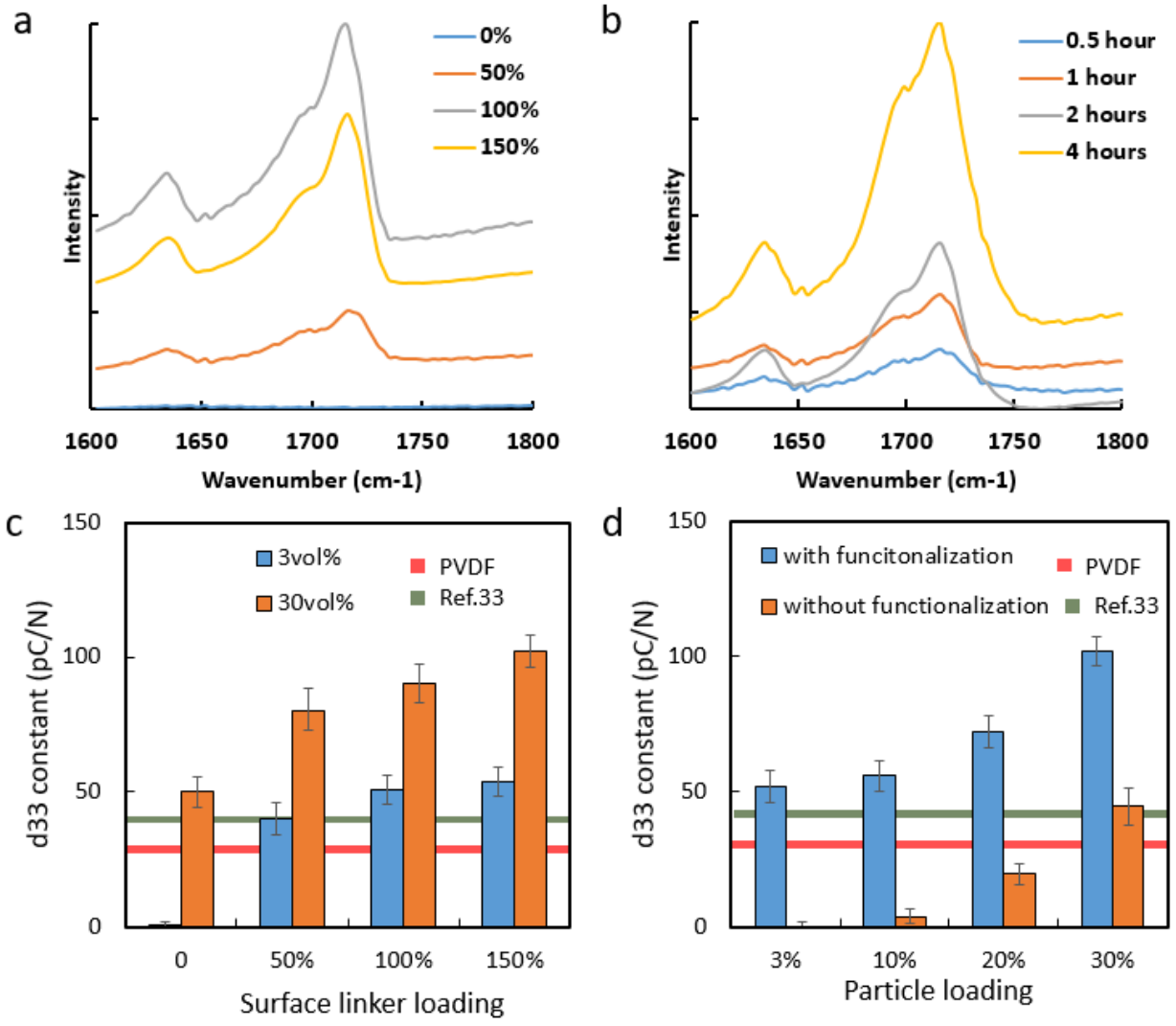

Figure S8| a) Fourier-transform infrared spectroscopy (FTIR) result showing the effects of different TMSPM loading. b) FTIR result showing the effects of reaction time on the surface functionalization, peaks around 4hrs. c) *d* constant as a function of the surface linker loading for functionalization of PZT nanoparticles. d) Comparison of *d* constant as a function of PZT nanoparticle volume loading percentage under two conditions: with functionalization and without functionalization.

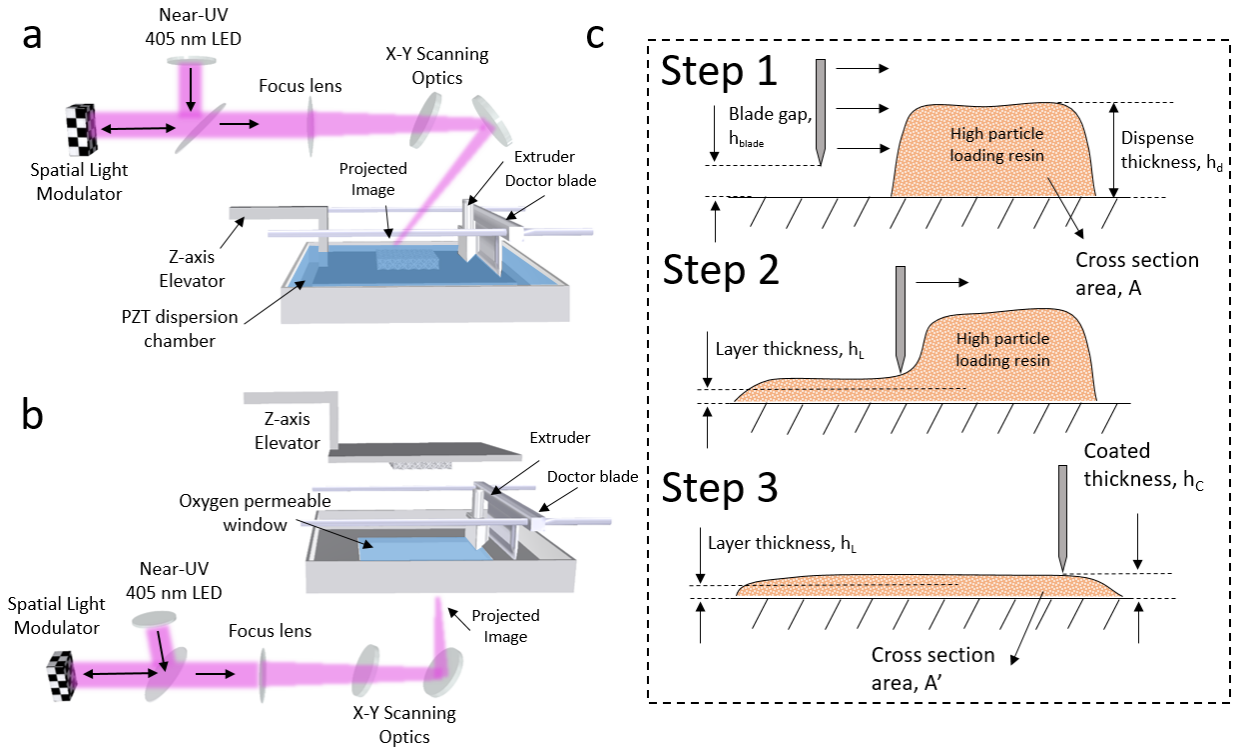

Figure S9| a-b) Schematics of the projection stereolithography systems used in our study with resin dispensing and flattening setup for a range of functional material loadings. c) Three steps during the recoating process.

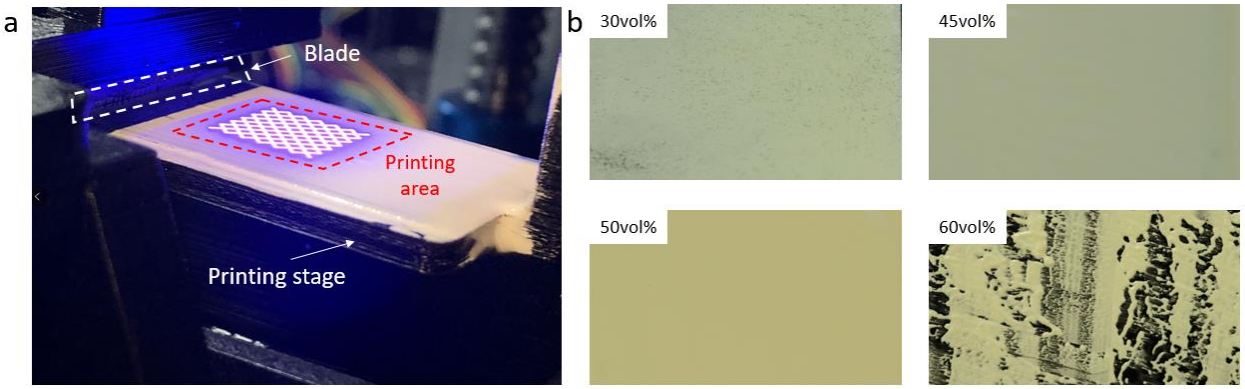

Figure S10| (a) Camera image of an as-cast uniform piezoelectric photosensitive resin film for Projection Micro-stereolithography; doctor blade height is 100µm. (b) Optical image of as-coated piezoelectric photosensitive resin films with different particle loadings.

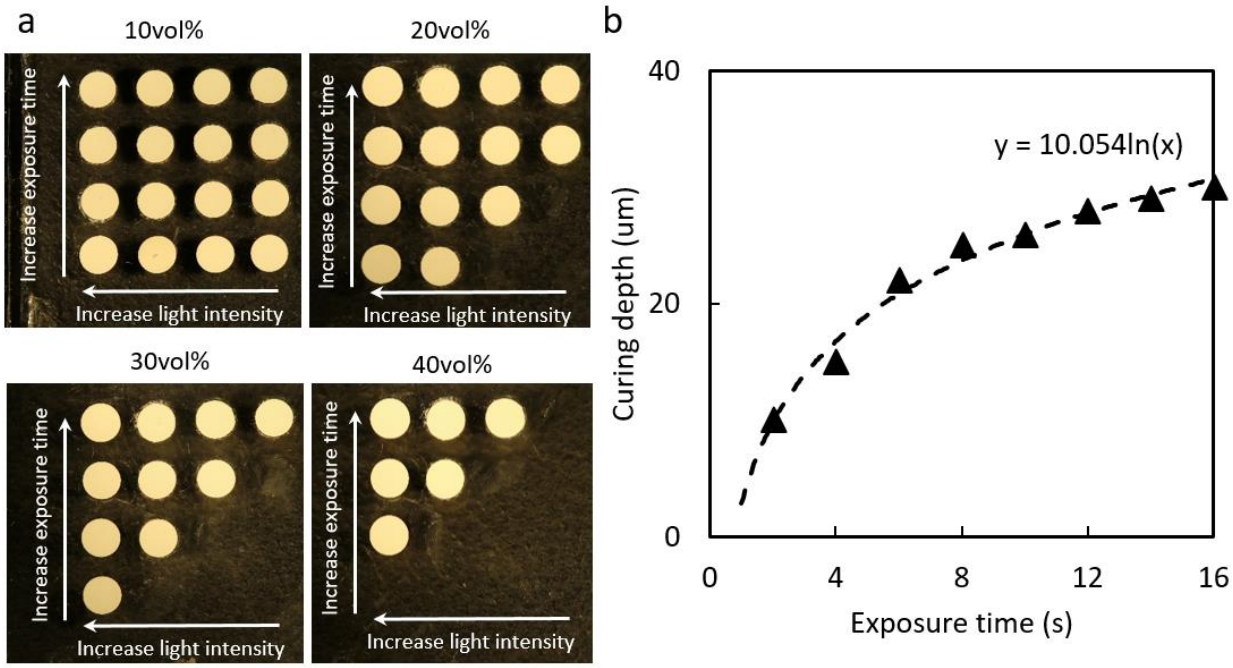

Figure S11| a) Optical images showing the curing depth of resins with 10vol%, 20vol%, 30vol% and 40vol% particle loadings. b) Curing depth of the 40vol% loading resin as a function of the exposure time.

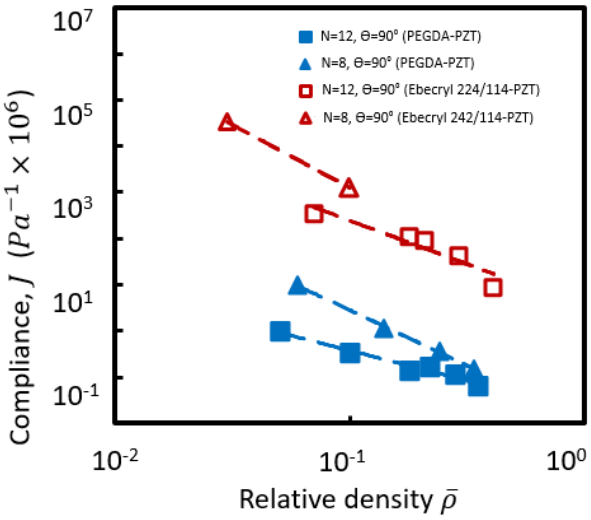

Figure S12| The tunable elastic compliance as a function of the relative densities.

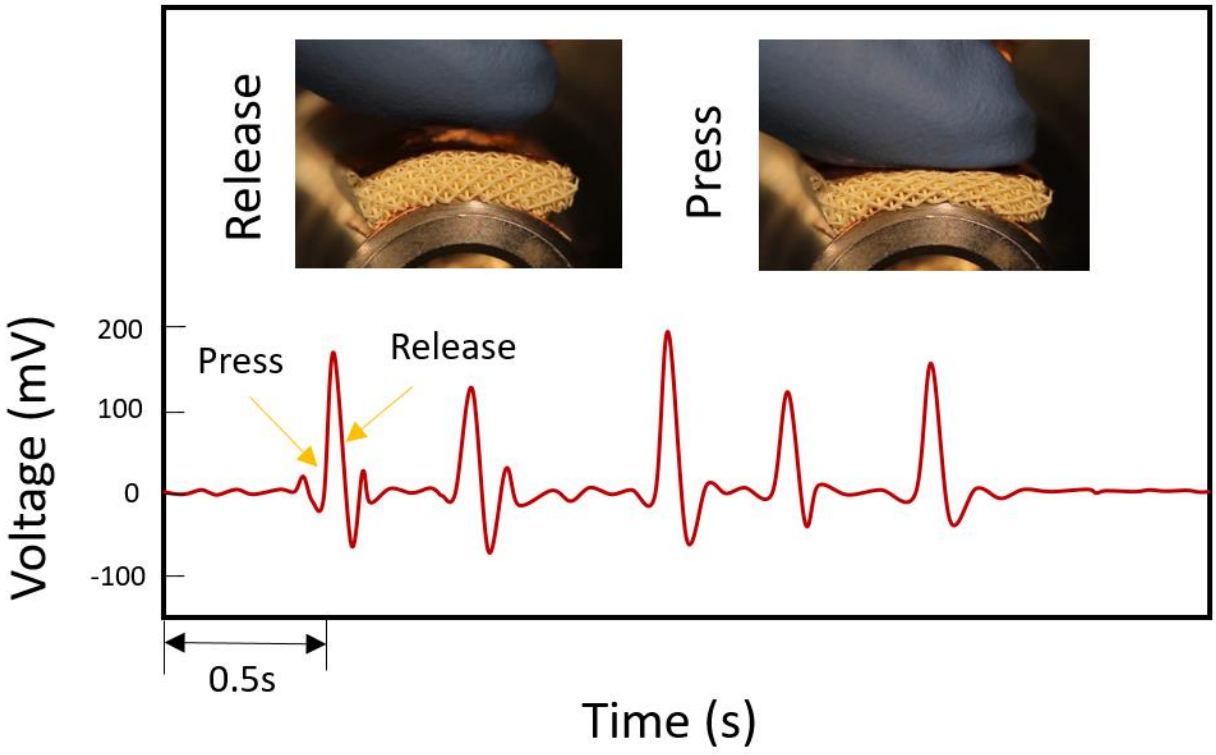

Figure S13| Hand tapping induced voltage response of the N=12 flexible piezoelectric metamaterial conformally attached onto a curved surface.

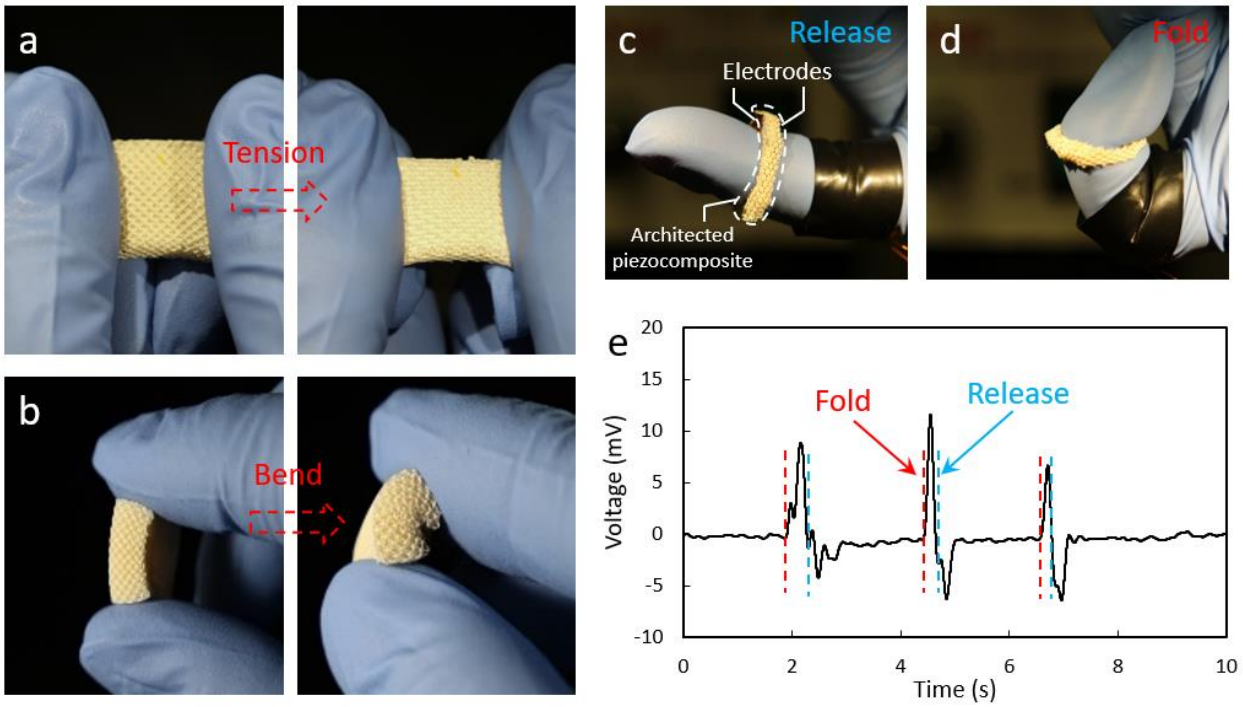

Figure S14| a~b) The optical images of the flexible 3D architected piezoelectric composite sensor with the N=12, Θ=90° structural design. Tensile and bending forces are applied to the lattice by fingers, showing the mechanical flexibility. c~d) A ring-like flexible 3D architected sensor attached on the finger. The sensor is compressed during the "fold" status of the finger. e) Voltage generated from the sensor during three cycles of finger folding and unfolding.

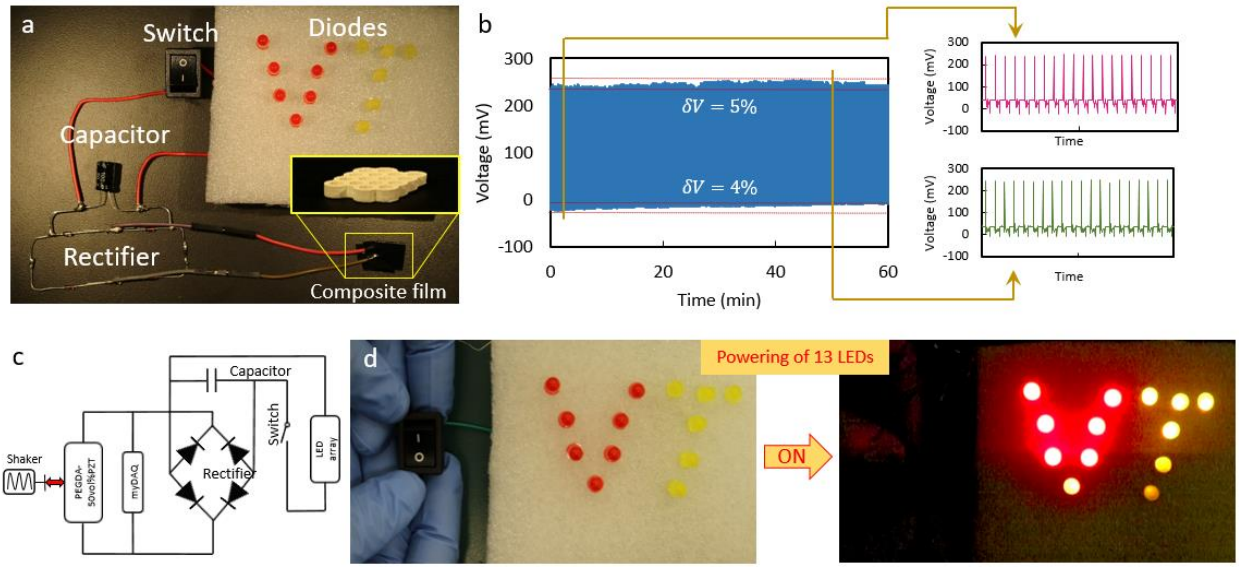

Figure S15| Energy Harvesting Experiment a) Camera image of the energy harvesting setup with architected piezoelectric metamaterial film. b) Energy generation and stability of the generator over time with voltage output. The result of the voltage output durability test over 60 min for verification of the energy harvesting stability. The magnified views of the regions highlighted by yellow lines represent clear and stable generated output voltage from the energy harvester. c) Schematic circuit diagram for measuring the output performance of the energy harvester. d) A photograph of the LED sign board with 13 high-intensity LEDs powered by the energy harvester.

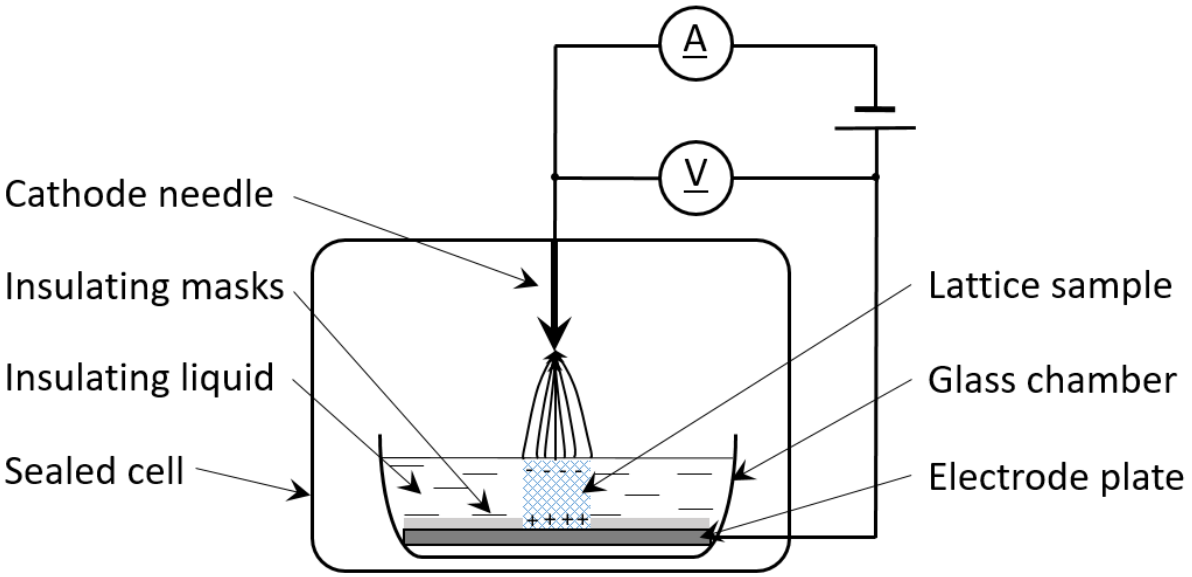

Figure S16| Schematic of the experimental setup for the corona poling.

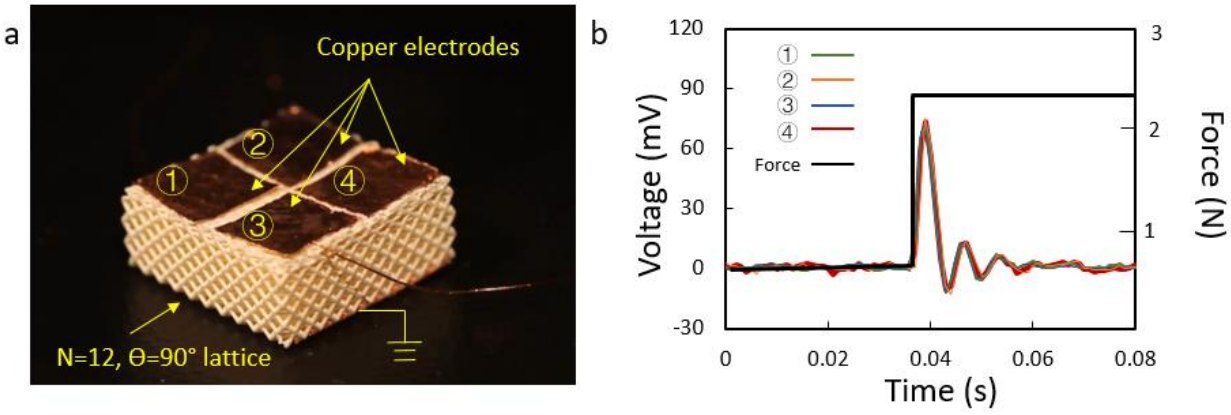

Figure S17| a) Optical image of the N=12, Θ=90º lattice with 4 electrodes attached at different positions. b) Voltage output on the 4 electrodes as a function of time.

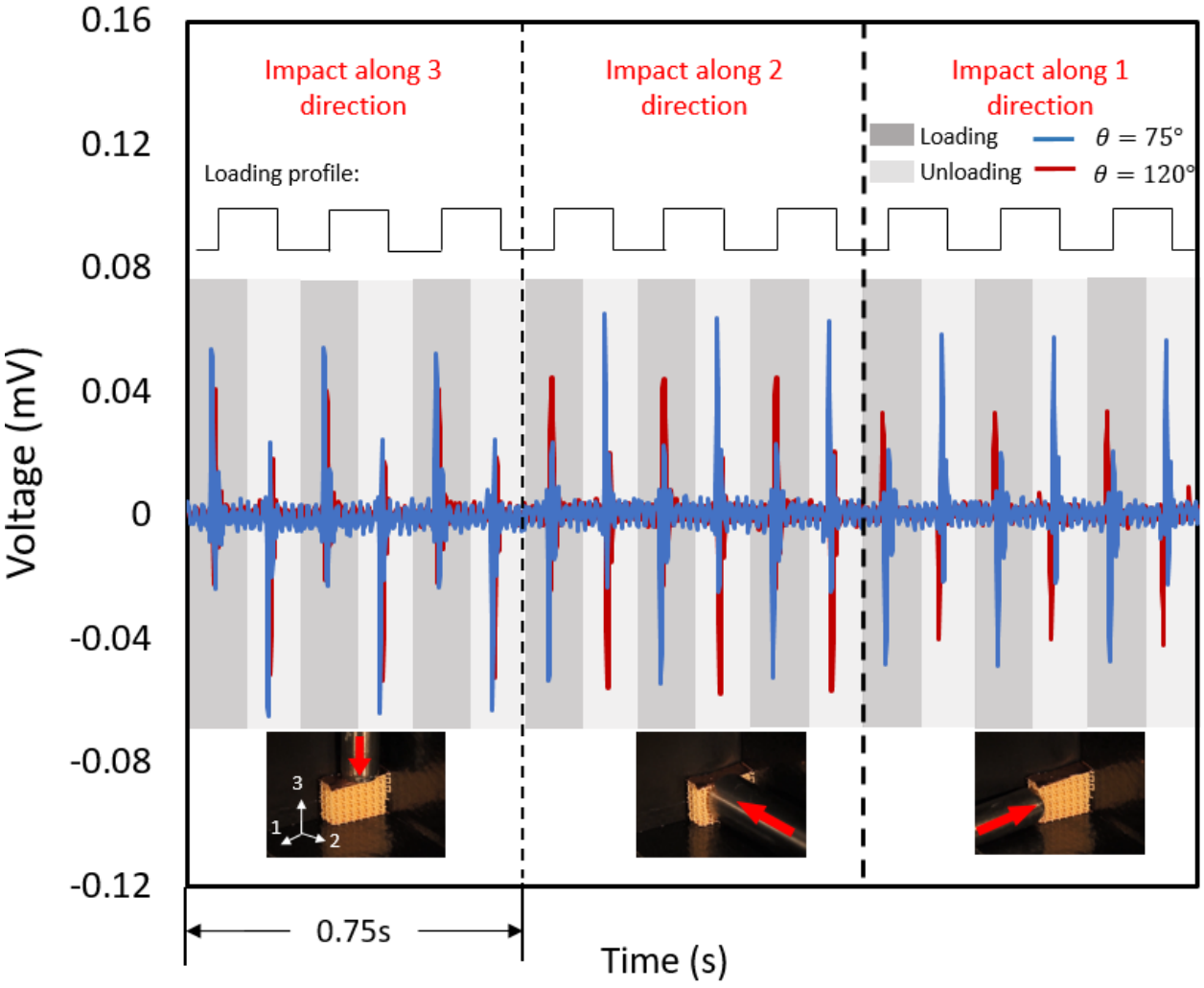

Figure S18| Real-time loading and release voltage outputs of two N=5 designs [$\bar{d}_{3M}$: {- - +}, $\bar{d}_{3M}$: {+ + +} respectively], with square loading profile stimulated from different directions. All samples are polled against 3 direction.

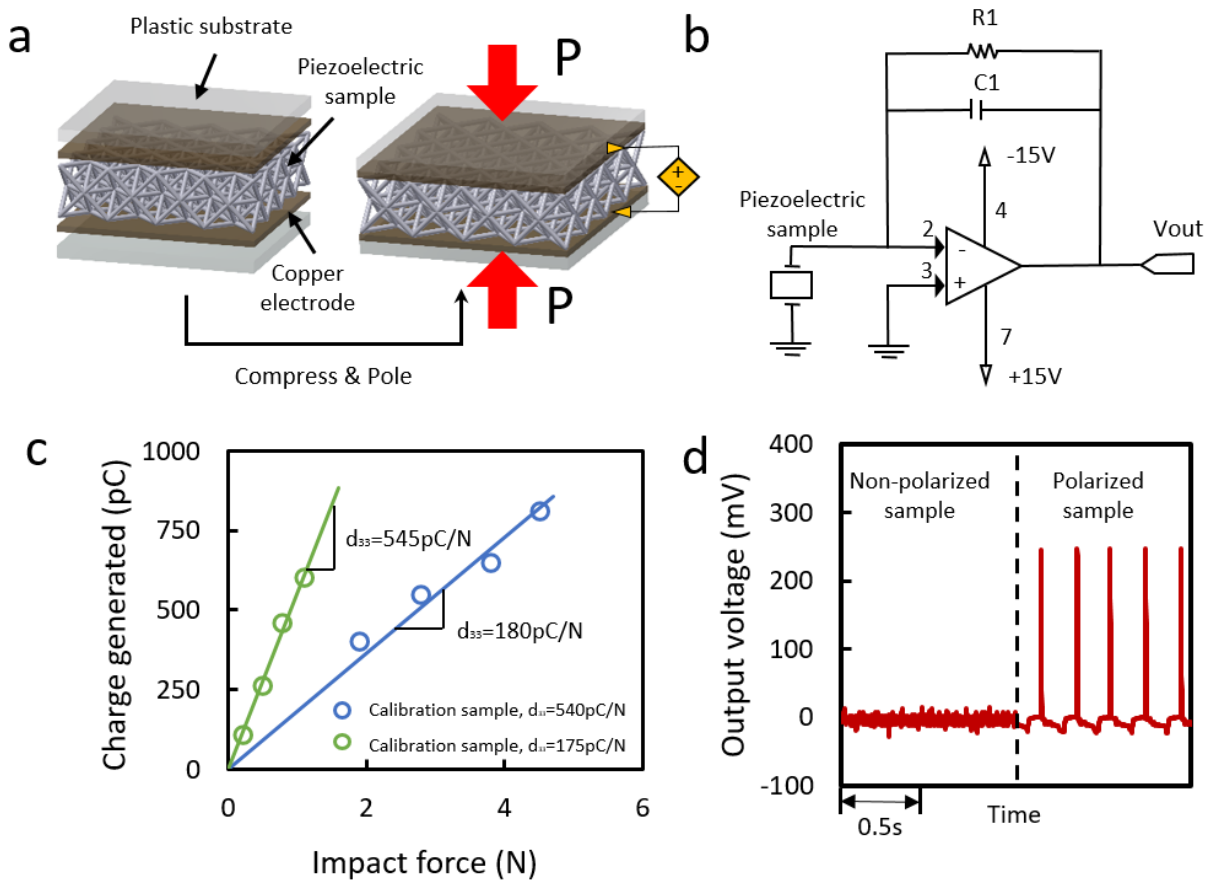

Figure S19| Direct piezoelectric coefficient testing and system calibration (a) Schematics of the system setup for measuring piezoelectricity on the as-fabricated architected metamaterials. (b) Circuit diagram for measuring the charges generated from the sample with applied stress. Electric charges generated from the piezoelectric metamaterial are collected by the capacitor, C1 (100pF). The output voltage, V_{out}, is measured through a data acquisition system (NI myDAQ) via R1 (40M Ω). The piezoelectric coefficients of the metamaterials are calculated from $d = (V_{out} \times 100pF)/F_{applied}$. (c) Charge versus applied force plot of two piezoelectric material samples as calibration of the testing fixture whose piezoelectric charge constants are measured by a piezo d_{33} test system (APC International, Ltd. Piezo d_{33} Test System). (d) Voltage output of non-polarized sample and polarized sample under ~0.5N compressive force.

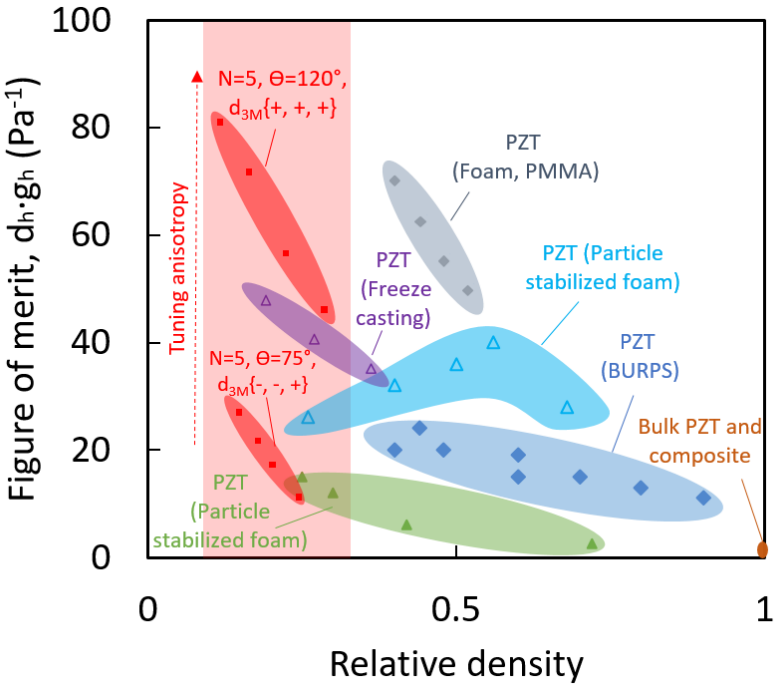

Figure S20| FOM of porous and bulk piezoelectric materials.

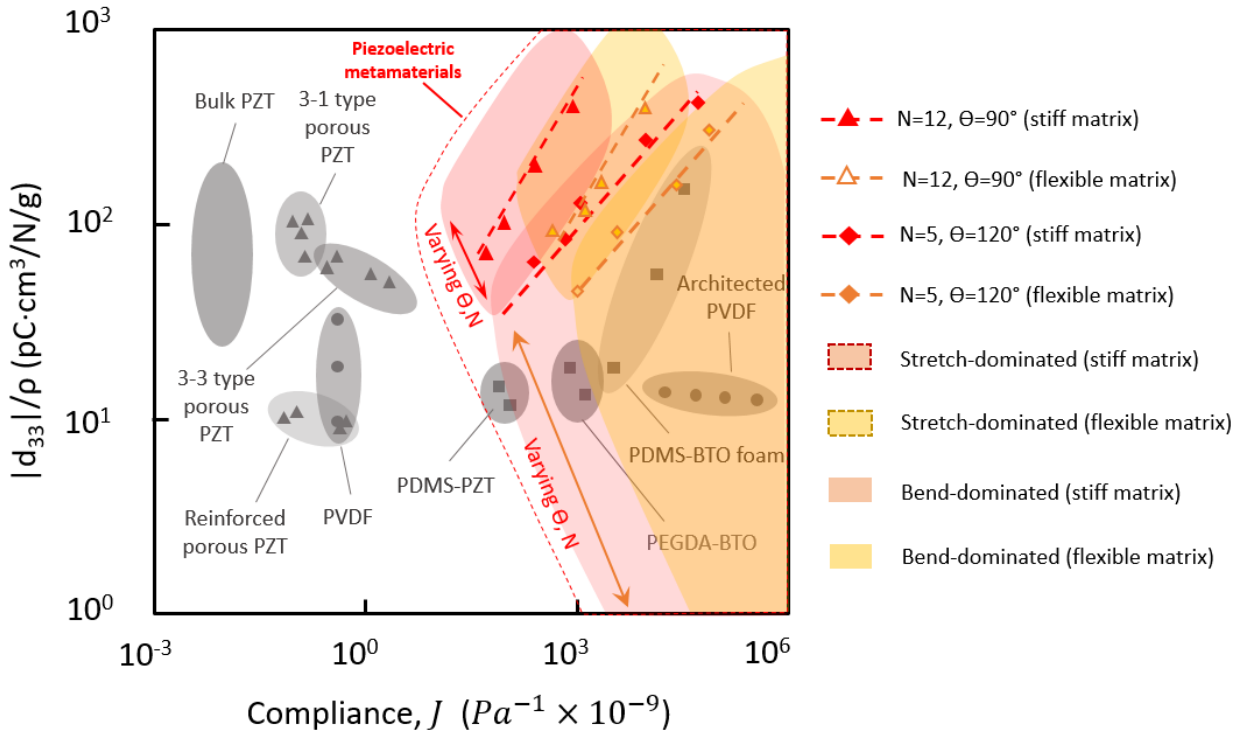

Figure S21| Comparison of specific piezoelectric charge coefficients and tunable elastic compliance between the piezoelectric metamaterials presented in this study and typical piezoelectric materials.

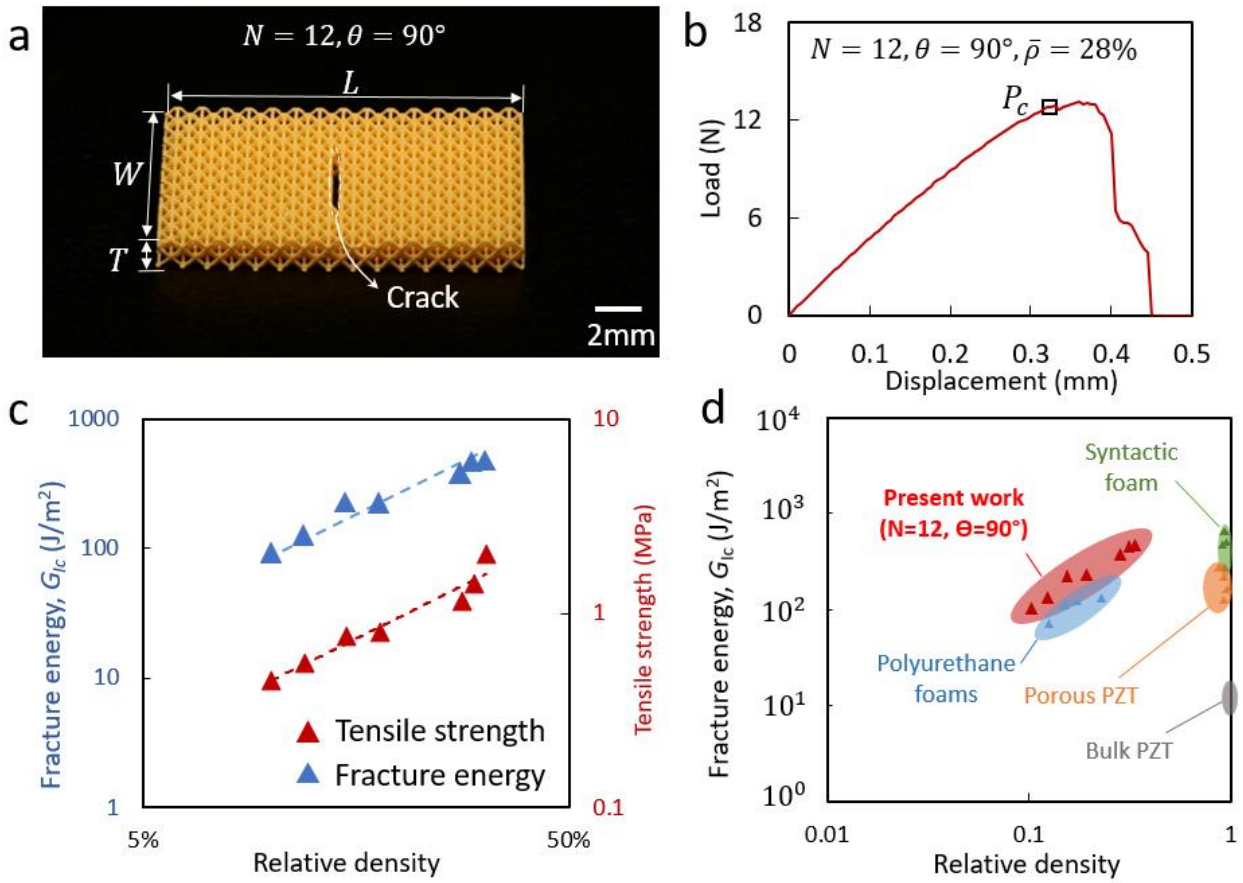

Figure S22| a) Optical image of a piezoelectric sample (N=12, Θ=90°, 28% relative density) with a central crack for fracture toughness testing. b) Load vs. Displacement curve of the CCT sample with N=12, Θ=90° and 28% relative density. c) Fracture energy and tensile strength of the piezoelectric metamaterial as a function of relative density. d) Material selection chart for the fracture energy versus relative density for a few available porous materials.

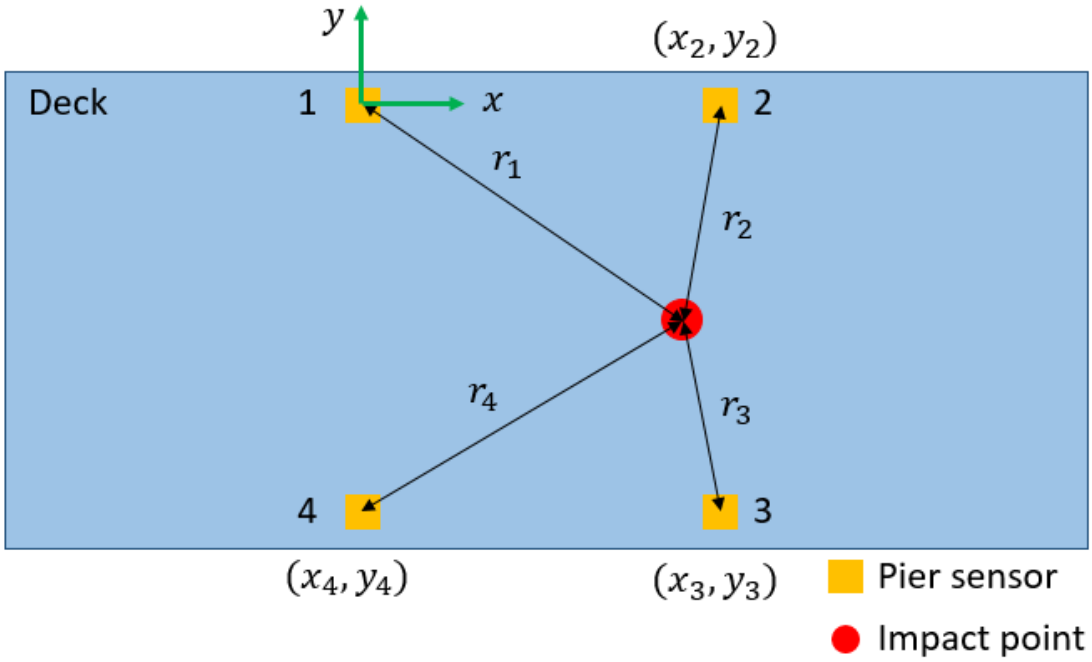

Figure S23| Geometric relationship between impact point and pier locations for determining the location of the impact point.

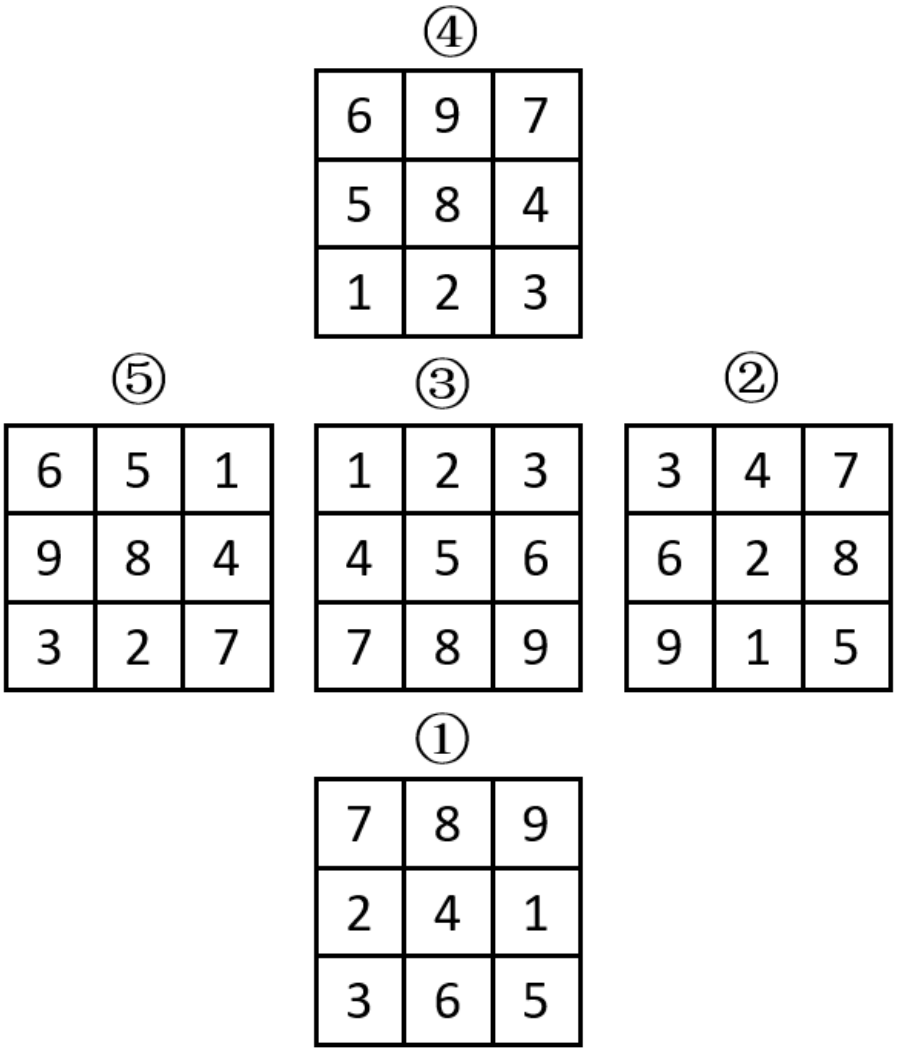

Figure S24| Schematics of the wiring method of the spatial stacking of multiple piezoelectric building blocks. The 25 building blocks are connected to 9 voltage channels of a data acquisition system (NI USB-6356). The blocks labeled as the same number are parallel and connected to the same voltage channel.

Table S1 Normalized d_{3M} distributions

Projection patterns	θ	$\bar{d}_{33}$	$\bar{d}_{32}$	$\bar{d}_{31}$
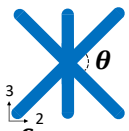 6-strut (3+3)	 100°	~0.93	~ -0.26	~ -0.26
	 90°	~0.98	~ -0.12	~ -0.12
	 60°	~0.99	~ -0.02	~ -0.02
	 30°	~ -0.99	~ 0.10	~ 0.10
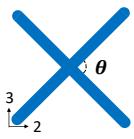 4-strut	 100°	~0.87	~0.35	~0.35
	 90°	~0.81	~0.41	~0.41
	 60°	~0.7	~0.5	~0.5
	 20°	~ -0.48	~ -0.62	~ -0.62
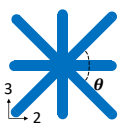 8-strut (4+4)	 100°	~0.99	~ -0.12	~ -0.12
	 90°	~1	~0	~0
	 60°	~0.75	~ -0.47	~ -0.47
	 45°	~0.89	~ -0.32	~ -0.32

Projection patterns	θ_1, θ_2	$\bar{d}_{33}$	$\bar{d}_{32}$	$\bar{d}_{31}$
3-strut (dissimilar projection patterns)	 $\theta_1 = 120^\circ, \theta_2 = 100^\circ$	~0.8	~0.39	~0.45
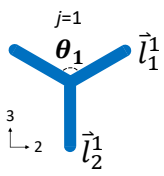	 $\theta_1 = 120^\circ, \theta_2 = 90^\circ$	~0.8	~0.32	~0.5
	 $\theta_1 = 120^\circ, \theta_2 = 45^\circ$	~0.8	~0.18	~0.56
	 $\theta_1 = 120^\circ, \theta_2 = 30^\circ$	~0.78	~0.09	~0.62
6-strut (dissimilar projection patterns)	 $\theta_1 = 90^\circ, \theta_2 = 80^\circ$	~0.93	~ -0.25	~ -0.23
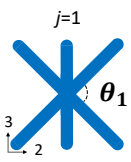	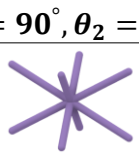 $\theta_1 = 90^\circ, \theta_2 = 60^\circ$	~ 0.89	~ -0.40	~ -0.16
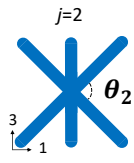	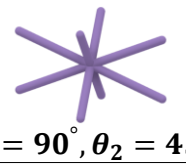 $\theta_1 = 90^\circ, \theta_2 = 45^\circ$	~ 0.85	~ -0.51	~ -0.08
	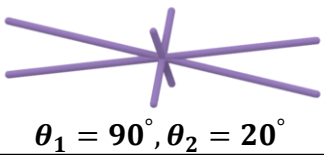 $\theta_1 = 90^\circ, \theta_2 = 20^\circ$	~ -0.55	~ -0.82	~ 0.11
3-strut/5-strut (dissimilar projection patterns)	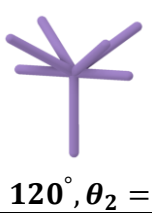 $\theta_1 = 120^\circ, \theta_2 = 30^\circ$	~0.99	~ -0.1	~0.01
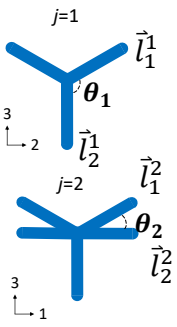	 $\theta_1 = 75^\circ, \theta_2 = -15^\circ$	~ 0.56	~ -0.73	~ -0.39

Table S2 Properties of the PZT particles used in the piezoelectric composite

Relative dielectric constant	1900
Dielectric dissipation factor (tand)	<2.00
k_p	0.63
k_{33}	0.72
k_{31}	0.36
k_{15}	0.68
d_{33}	400
$-d_{31}$	175
d_{15}	590
g_{33}	24.8
g_{31}	12.4
g_{15}	36.0
Young's modulus Y_{11}	6.3
Y_{33}	5.4

Table S3 Measurement of compliance against relative density of the piezoelectric metamaterials

Relative Density	Modulus(MPa)	Compliance(1/MPa)
0.35	15	0.06
0.28	9	0.11
0.22	6	0.16
0.18	7	0.14
0.1	3	0.33
0.05	1	1
0.34	6.5	0.15
0.24	2.8	0.35
0.14	0.9	1.11
0.06	0.1	10
0.41	0.11	8.84
0.29	0.02	43.80
0.21	0.01	91.85
0.18	0.009	111.11
0.07	0.003	333.33
0.1	0.0008	1250
0.03	0.00003	33333.33

Table S4 Measurement of piezoelectric charge and voltage constant against relative density

Polymer matrix	Design	Relative density	Voltage (V)	Charge (pC)	Force (N)	d33 (pC/N)
Stiff matrix	N=12, Θ=90°	0.05	0.039	3.9	0.1	40.5
			0.083	8.3	0.2	
			0.123	12.3	0.3	
		0.19	0.0415	4.15	0.1	42
			0.084	8.4	0.2	
			0.1275	12.75	0.3	
		0.28	0.044	4.4	0.1	43.5
			0.087	8.7	0.2	
			0.129	12.9	0.3	
		0.38	0.0445	4.45	0.1	44.5
			0.09	9	0.2	
			0.132	13.2	0.3	
		0.45	0.046	4.6	0.1	45
			0.088	8.8	0.2	
			0.135	13.5	0.3	
Stiff matrix	N=5, Θ=120°	0.05	0.0265	2.65	0.1	27.2
			0.054	5.4	0.2	
			0.084	8.4	0.3	
		0.15	0.028	2.8	0.1	28.5
			0.0568	5.68	0.2	
			0.087	8.7	0.3	
		0.25	0.031	3.1	0.1	31.2
			0.0624	6.24	0.2	
			0.0942	9.42	0.3	
		0.35	0.0316	3.16	0.1	31.4
			0.062	6.2	0.2	
			0.0951	9.51	0.3	
		0.45	0.0321	3.21	0.1	32.1
			0.0634	6.34	0.2	
			0.0975	9.75	0.3	
Flexible matrix	N=12, Θ=90°	0.05	0.043	4.3	0.1	44.5
			0.091	9.1	0.2	
			0.135	13.5	0.3	
		0.19	0.0455	4.55	0.1	46
			0.092	9.2	0.2	
			0.1395	13.95	0.3	
		0.28	0.048	4.8	0.1	47.5
			0.095	9.5	0.2	
			0.141	14.1	0.3	
		0.38	0.0485	4.85	0.1	48.5
			0.098	9.8	0.2	
			0.144	14.4	0.3	
		0.45	0.05	5	0.1	49
			0.096	9.6	0.2	
			0.147	14.7	0.3	
Flexible matrix	N=5, Θ=120°	0.05	0.0305	3.05	0.1	31.2
			0.062	6.2	0.2	
			0.096	9.6	0.3	
		0.15	0.032	3.2	0.1	32.4
			0.0648	6.48	0.2	
			0.099	9.9	0.3	
		0.25	0.035	3.5	0.1	35.2
			0.0704	7.04	0.2	
			0.1062	10.62	0.3	
		0.35	0.0356	3.56	0.1	35.4
			0.07	7	0.2	
			0.1071	10.71	0.3	
		0.45	0.0361	3.61	0.1	36.1
			0.0714	7.14	0.2	
			0.1095	10.95	0.3	

*Functionalized particle loading: 2.5vol% (16wt%)

Stiff matrix	N=12, Θ=90°	0.28	0.096	9.6	0.15	62
			0.13	13	0.2	
			0.148	14.8	0.25	
			0.176	17.6	0.3	
		0.33	0.288	28.8	0.45	68
			0.225	22.5	0.36	
			0.162	16.2	0.3	
			0.09	9	0.18	
		0.38	0.11	11	0.15	72
			0.14	14	0.2	
			0.17	17	0.25	
			0.23	23	0.3	
		0.45	0.072	7.2	0.1	76
			0.09	9	0.15	
			0.144	14.4	0.25	
			0.216	21.6	0.35	
Flexible matrix	N=8, Θ=90°	0.32	0.04	4	0.1	36
			0.056	5.6	0.15	
			0.076	7.6	0.2	
		0.4	0.04	4	0.1	38
			0.06	6	0.15	
			0.07	7	0.2	
		0.45	0.04	4	0.1	42
			0.07	7	0.15	
			0.095	9.5	0.2	

*Functionalized particle loading: 30vol% (88wt%)

Table S5 Piezoelectric coefficient of the bulk functionalized PZT nanocomposite

Composition \ Piezoelectric charge constant(pC/N)	d_{31}	d_{32}	d_{33}
PEGDA-2.5vol%PZT	-15	-15	52
PEGDA-36vol%PZT	-26	-26	90
Ebecryl 242/114-2.5vol%PZT	-10	-10	55